Curvature regulates subcellular organelle location to control intracellular signal propagation

Authors: Rhodora C. Calizo[1], Amit Ron[2], Mufeng Hu[2], Smiti Bhattacharya[2], William G.M. Janssen[1], James Hone[2], Suzanne Scarlata[3], Padmini Rangamani[4]*, Ravi Iyengar [1]*

One Sentence Summary: Changes in the global curvature of the plasma membrane alter the distances between the plasma membrane and sarcoplasmic reticulum, and the nucleus, and modulate the strength of Ca^{2+} signaling in vascular smooth muscle cells.

Affiliations:

[1] Department of Pharmacological Sciences and Systems Biology Center New York, Icahn School of Medicine at Mount Sinai, New York, NY 10029

[2]Department of Mechanical Engineering, Columbia University, New York, NY 10027.

[3]Department of Chemistry and Biochemistry, Worcester Polytechnic Institute, Worcester, MA 01609.

[4]Department of Mechanical and Aerospace Engineering, University of California San Diego, La Jolla, CA 92093.

* Joint senior authors

Address correspondence to:

Ravi Iyengar, Ph.D.
Department of Pharmacological Sciences
Icahn School of Medicine at Mount Sinai
One Gustave L. Levy Place, Box 1215
New York NY 10029
Phone: 212-659-1707
Fax: 212-831-0114
e-mail: ravi.iyengar@mssm.edu

or

Padmini Rangamani, Ph.D.
Department of Mechanical and Aerospace Engineering
University of California San Diego
La Jolla, CA 92093
Phone: 858-534-4734
e-mail: prangamani@ucsd.edu

ABSTRACT

The shape of cell is intimately connected to its function; however, we do not fully understand the underlying mechanism by which global shape regulates cell functions. Here, using a combination of theory, experiments and simulation, we investigated how global cell curvature can affect numerous subcellular activities and organization to control signal flow needed for phenotypic function. We find that global cell curvature regulates organelle location, inter-organelle distances and differential distribution of receptors in the plasma membrane. A combination of these factors leads to the modulation of signals transduced by the M_3 muscarinic receptor/G_q/PLCβ pathway at the plasma membrane, amplifying Ca^{2+} dynamics in the cytoplasm and the nucleus as determined by increased activity of myosin light chain kinase in the cytoplasm and enhanced nuclear localization of the transcription factor NFAT. Taken together, our observations show a systems level phenomenon whereby global cell curvature affects subcellular organization and signaling to enable expression of phenotype.

INTRODUCTION

Cells utilize receptors on the plasma membrane to transduce a range of extracellular signals to regulate function in the cytoplasm and the nucleus[1]. Reaction kinetics of the biochemical interactions that comprise the signaling networks regulate the temporal dynamics of activation and inactivation of signaling components and effectors[2]. However, information flow within cells is not just temporally regulated, it is also spatially regulated by the shape of the cell[3-5] and surface-to-volume ratio at the plasma membrane[6]. An additional layer of complexity is conferred by the spatial transfer of information by signaling reactions that occur within or at intracellular organelles. Recently, studies have shown that signaling at the endosomes plays an important role in prolonging cAMP dynamics through GPCRs[7] and in EGFR dynamics[8]. An important compartmental regulation of organelle-based signaling is Ca^{2+} dynamics, since endoplasmic/sarcoplasmic reticulum is a regulatable Ca^{2+} store in cells. Ca^{2+} is a ubiquitous signaling molecule that controls many cellular functions including fertilization, proliferation, migration and cell death[9-12]. Ca^{2+} is able to participate in controlling this diverse array of functions due to the precise control of Ca^{2+} concentration across the cell. In vascular smooth muscle cells (VSMC), Ca^{2+} regulates both contractility and gene expression through IP_3-mediated Ca^{2+} release by IP_3R receptors located on the membrane of the sarcoplasmic reticulum (SR) and through Ca^{2+} influx at the plasma membrane[13-15]. Ca^{2+}-calmodulin activates myosin light chain kinase (MLCK), which phosphorylates the light chain of myosin, initiating contraction[16]. Ca^{2+} also activates protein kinases and phosphatases that regulate transcription regulators that define the phenotypic status of VSMC[17]. Ca^{2+} activates calcineurin, which dephosphorylates the transcription factor nuclear factor of activated T-cells (NFAT) in the cytoplasm, resulting in its nuclear accumulation and expression of NFAT-regulated genes[18]. Ca^{2+} also activates calmodulin kinase II (CaMKII), that phosphorylates the transcription factor serum response factor (SRF)[19] which, as a complex with myocardin, controls the expression of proteins necessary for the contractile function of VSMC[20].

VSMC in the medial layer of blood vessels are not terminally differentiated and can undergo phenotypic transitions during injury and disease states[21-23]. VSMC shape and function are closely related; increasing elongation or aspect ratio (AR, defined as the ratio of the short axis to long axis) is correlated with differentiation and contractility[24, 25]. How cell elongation is mechanistically linked to contractility is poorly understood. Based on the observations that cell shape and Ca^{2+} signaling closely regulate the contractile phenotype of differentiated VSMCs, we hypothesized that cell shape regulates organelle location, including the relative distances between plasma membrane, endoplasmic/sarcoplasmic reticulum (ER/SR) and the nucleus, to modulate cellular function. In other words, we sought to answer the question -- how does cell shape dependent organelle localization drive spatial control of information transfer? The answer to this question is critical for understanding how mechanochemical relationships control cell shape, signaling, and phenotype. We used micropatterned substrates to culture VSMCs in different shapes and developed theoretical and computational models to represent the spatio-temporal dynamics of Ca^{2+} transients mediated by Muscarinic Receptor 3 (M_3R)/Phospholipase Cβ (PLCβ) pathway. Activation of M_3R mediates contractility in VSMC by activating PLCβ resulting in phosphoinositide hydrolysis and IP_3 mediated Ca^{2+} release from the SR[26, 27]. Our studies show an unexpected modulation of organelle location as a function of membrane curvature and that this change in organelle location results in signal amplification in the cytoplasm and nucleus.

RESULTS

Reaction-Diffusion model predicts that the distance between PM and SR membrane affects signaling dynamics in the cytoplasmic volume.

We tested the hypothesis that a change in membrane curvature and distance between two membranes affects signaling dynamics using a phenomenological reaction-diffusion model (Fig. 1a). A signaling molecule of interest, A, is produced at the PM with an on-rate k_{on} (1/s) and binds to a receptor located at the SR membrane, with a rate k_{off} (1/s) and is free to diffuse in the sandwiched cytoplasmic space and is degraded by a degrading enzyme with a rate k_{deg} (1/s). This model essentially captures the lifecycle of a second messenger such as IP_3 that is produced at the PM through PIP_2 hydrolysis by phospholipases, binds to inositol 3 phosphate receptor (IP_3R) channel at the SR membrane and is degraded in the cytoplasm by 1,4,5-trisphosphate-5-phosphatase[28]. These events can be mathematically represented by the following system of reaction-diffusion equations. The dynamics of A in the cytoplasm are governed by diffusion and degradation and is given by,

$$\frac{\partial C_A}{\partial t} = D\nabla^2 C_A - k_{deg} C_A \qquad \text{Eq. (1)}$$

Here, D is the diffusion coefficient of A ($\mu m^2/s$), and C_A is the concentration of A (μM). The boundary condition at the PM is a balance between the rate of production of A at the membrane and the diffusive flux from the membrane to the cellular interior and is given by,

$$D(\mathbf{n} \cdot \nabla C_A)|_{PM} = k_{on} C_A|_{PM} \qquad \text{Eq. (2)}$$

Here, n is the normal vector to the surface and ∇ represents the gradient operator. At the SR membrane, similarly, we can write the boundary condition for the consumption of A as the balance of diffusive flux to the SR and consumption rate at the SR.

$$-D(\mathbf{n} \cdot \nabla C_A)|_{SR} = k_{off} C_A|_{SR} \qquad \text{Eq. (3)}$$

We solved these equations using finite element methods on three geometries (1) a rectangle (constant distance, zero curvature) (2) a circle, (constant distance, constant curvature) and (3) an elliptical sector, (varying distance, varying curvature) (Fig. 1b). In cases (1-2), the gradient of A is only along the radial direction (Fig. 1c). In triangular and trapezoidal geometries, varying PM-SR gradients result in two-dimensional gradients (Supplementary Fig. 1). However in case (3), the curvature of the membrane and the PM-SR distance will affect both the production and consumption of A at the PM and SR respectively. Hence, A varies both in the radial and angular directions, indicating that curvature and varying distances between the two membranes amplifies signaling gradients.

We next conducted dimensional analysis to identify when the dynamics of A would be diffusion-dominated or reaction-dominated. Non-dimensionalization of Eq. 1 results in a dimensionless group $D/(k_{deg}L^2)$, the Damkohler number[29]. This dimensionless number is the ratio of diffusion time scale to reaction time scale. We found that the dynamics of A are diffusion dominated for physiological values of k_{deg} (Fig. 1d). Increasing k_{deg} many-fold or reducing the diffusion constant of A can result in the dynamics of A being reaction dominated for different PM-SR

distances (Fig. 1d, shaded blue region). Both the increase in k_{deg} and the decrease in D, to obtain reaction-dominated regimes, are out of the range of physiological values, suggesting that the dynamics of A in the sandwiched space between the PM and SR are primarily diffusion dominated. From this simple phenomenological model, we predict that second messenger signaling networks such as IP_3, where signaling occurs between PM and SR, will be impacted by global curvature and distance between the PM and the SR. This prediction raises the following questions: (1) does cell shape affect PM-SR distance? (2) Does changing PM-SR distance affect intracellular signaling dynamics? And (3) what is the impact of changing distance between organelles on signaling dynamics? We used VSMCs grown on micropatterned substrates to answer these questions.

Cell shape affects cytoskeleton organization and organelle location

We determined if changing cell shape affects organelle distribution and in particular PM-SR distance. In order to control the large scale cell shape, we used micropatterned substrates with the same surface area but increasing aspect ratio (AR, circles 1:1 to ellipses 1:8) (Fig. 2a). We investigated how cell shape affects cytoskeletal organization since the two are tightly interwoven[30-32]. Actin stress fibers increasingly oriented themselves along the long axis of the cell as the aspect ratio increased (Fig. 2b), indicating that the cells were responding to the mechanical forces and tension exerted by the substrate[33]. Microtubules became highly aligned and increasingly sparser in the cell tips compared to the cell body as the cell aspect ratio increased (Supplementary Fig. 2). Because cytoskeletal organization plays an important role in organelle distribution[34, 35], we visualized the effect of cell shape on the bulk distribution and location of the mitochondria (Supplementary Fig. 3), endosomes (Supplementary Fig. 4) and Golgi membrane (Supplementary Fig. 5). These organelles increasingly localized to the cell center (perinuclear region) with increasing aspect ratio, similar to the characteristic central distribution of the endomembrane system in well-differentiated VSMC[24]. Because SR stores Ca^{2+}, which controls both excitation-transcription coupling and contractility in VSMC[36], we focused on SR distribution as a function of cell shape, using calnexin (Fig. 2c), protein disulfide isomerase (Fig. 2d), reticulon-4 (Fig. 2e) and bodipy glibenclamide (Supplementary Fig. 6) as SR markers. All four markers show that in circular cells, the SR was spread uniformly throughout the cell; increased aspect ratio induced the SR to localize in the perinuclear region and become significantly sparser, and mainly tubular, in the cell tips (Fig. 2c-e, Supplementary Fig. 6). Upon close inspection of Airy scan images of these SR markers, we qualitatively observe that in circular cells, the SR appeared to be equidistant from the plasma membrane along the periphery, i.e. there were no angular variations of PM-SR distance, while elliptical cells show a large angular variation in the PM-SR distance (Fig. 2d-e bottom panels and Supplementary Fig. 6, inset). We used transmission electron microscopy (TEM) to quantitatively confirm that the PM-SR distance is shape dependent. The cell periphery of circular cells and the cell body of elliptical cells showed long patches of smooth SR that were positioned close to the plasma membrane. PM-SR distance was indeed dependent on the shape of the cell: PM-SR distance in cell body of elliptical cells was significantly smaller compared to circular cells (Fig. 2g). In the tips of elliptical cells, the SR membrane formed fewer contacts with the plasma membrane, and showed significantly higher PM-SR distance (Fig. 2g). These results are consistent with the recent observation in neurons that PM-ER contacts are more extensive in the cell body compared to elongated projections such as dendrites and axons[37]. While other groups have reported that cell shape can affect organelle location[38, 39], to our knowledge, this is the first quantitative

characterization of PM-SR distances and the SR abundance along the juxtamembrane region with controlled cell shape variation. We then determined the relationship between global cell shape and distances between the nucleus and various organelles in VSMC. Nuclear aspect ratio increased with cellular aspect ratio (Fig. 2i) while nuclear size (area μm^2) decreased with increasing cell aspect ratio (Fig. 2j). The nucleus became increasingly oriented along the major axis of the cell as the whole-cell aspect ratio increased, evidenced by polar graphs showing the orientation histograms of nuclei of cells in increasing cell AR (Fig. 2k). Circular shaped cells showed a random nuclear orientation whereas increasing the cellular aspect ratio progressively oriented the nucleus in the geometric center of the cell. PM-nuclear distance in the major axis of the cell increased with cell aspect ratio (Fig. 2m) while the PM-nuclear distance in the minor axis decreased with cell aspect ratio (Fig. 2n). These results indicate that in VSMC, cell elongation resulted in nuclear elongation, reduced nuclear size, and a decrease in the PM-nuclear distance in the minor axis of the cell (*i.e.* near the center of the cell). Thus, we show that cell shape affects not only organelle location, but also affects PM-SR distance, nuclear shape and PM-nuclear distances.

Computational models predict that IP_3 spatio-temporal dynamics depend on nanometer scale changes in PM-SR distances.

We next asked if changing PM-SR distance will impact the dynamics of IP_3 in VSMCs. It is currently not possible to manipulate PM-SR distances with precise control in cells. Therefore, we developed a computational model for investigating how changing PM-SR distance would affect IP_3 dynamics. This model is composed of a system of multi-compartmental partial differential equations, representing the reaction-diffusion of cytoplasmic species in the volume, coupled with boundary fluxes at the membranes. The reactions capture the biochemical interactions from the ligand binding and activation of M_3R to IP_3 production by PLC-mediated hydrolysis of PIP_2 release from the SR (Fig. 3a, Supplementary Table 1). As before, we tested three different geometries – rectangles, circles, and ellipses. Each geometry consists of compartments representing the plasma membrane, the cytoplasm, the SR (modeled as thin rectangles) and the SR membrane (Fig. 3b). To test the effect of changing PM-SR distance on signaling dynamics independent of curvature, we computed the spatio-temporal profiles of IP_3 in rectangular geometries. We found that varying the PM-SR distance played a critical role in determining the dynamics of IP_3 (Fig. 3b, Supplementary Fig. 8). When the PM-SR distance is 50 nm, IP_3 is concentrated between the PM and the SR, but as the PM-SR distance increases, the IP_3 microdomain dissipates and no local increase in concentration is observed. Even in this highly idealized scenario, we find that there is a clear dependence of IP_3 spatio-temporal dynamics on PM-SR distance. Furthermore, the SR acts as a diffusion barrier for IP_3, preventing diffusion of IP_3 away from the PM-SR region. The dynamics of IP_3 in locations with and without SR (Fig. 3c) were also different, indicating that the diffusion distance set up by the PM-SR coupling plays an important role in governing the dynamics of second messengers such as IP_3 and potentially Ca^{2+}.

Next, we investigated the role of curvature coupling to PM-SR distances on IP_3 and dynamics. We designed geometries that represented circular cells or elliptical cells with distance parameters based on experimental measurements from TEM analyses (Fig. 2g). We investigated the role of PM-SR distance in circular geometries. Again, we modeled the SR as thin rectangles and this time placed the SR at 98 nm away from the PM based on the experimental measurements. We

found that the region between the PM and the SR acts as an IP_3 microdomain since the SR not only consumes IP_3 but also acts as a diffusion trap (Fig. 3e). However, we did not observe any angular variation along the periphery of the domain where the SR was present. We found that the angular variation for IP_3 and Ca^{2+} dynamics was a result of the presence or absence of SR (Fig. 3c). There is a small radial variation at early times because the SR act as diffusion barrier but over longer times, these cytoplasmic gradients disappear (See different time points in Fig. 3c).

We also conducted simulations for elliptical geometries with the SR at the variable distance from the PM as per experimental measurements such that the shortest PM-SR distance is 67 nm and the farthest PM-SR distance is more than 150 nm. This allowed us investigate how varying curvature and varying PM-SR distance affects IP_3 dynamics. We found that the curvature of the plasma membrane, coupled with variable PM-SR distance gave rise to variable IP_3 dynamics that was a function of PM-SR distance along the periphery (Fig. 3f). We found that the total amount of IP_3 produced over 5 min was higher in elliptical cells than in circular cells (Fig. 3g). Thus, our simulations indicate that PM-SR distance affects the IP_3 dynamics and curvature coupling serves to amplify this effect.

Cell shape affects receptor activation on the membrane and intracellular calcium dynamics

We tested the model predictions that distance between PM and SR can affect the dynamics of Ca^{2+} mediated by the $M_3R/IP_3/Ca^{2+}$ pathway[13, 40]. We stained for M_3R in circular and elliptical cells under three different conditions - unstimulated, stimulated with carbachol, and stimulated with carbachol in the presence of hypertonic sucrose, which inhibits receptor endocytosis[41-43]. In both the basal state and stimulated states, M_3R was uniformly distributed on the plasma membrane of both circular and elliptical cells (Supplementary Fig. 9). Interestingly, in elliptical cells, when M_3R was stimulated and endocytosis was inhibited, M_3R accumulated in the cell body compared to the cell tips while there was no observable spatial asymmetry in the distribution of M_3R in circular cells (Fig. 4a and Supplementary Fig. 9). We then investigated the effect of shape on cytoplasmic and nuclear Ca^{2+} dynamics upon stimulation of M_3R in patterned VSMC (Fig. 4b-c). In the cytoplasmic region, circular and elliptical showed similar peak Ca^{2+} amplitudes. However, elliptical cells showed a slower rate of decrease in Ca^{2+} compared to circular cells, resulting in a slightly higher temporally integrated Ca^{2+} compared to circular cells, although the differences were not statistically significant ($p=0.057$, two-tailed t-test). Since small changes in second messenger signals can have large functional effects by being amplified by signaling networks[44], we measured downstream myosin light chain kinase (MLCK) activity using a CaM-sensor FRET probe[45, 46] (Fig. 4e-g). Elliptical cells showed a higher degree of MLCK FRET probe localization on actin filaments (Fig. 4e) and higher maximal activation compared to circular cells (Fig. 4f-g), indicating that the shape-induced increase in cytoplasmic Ca^{2+} signal propagates and is amplified downstream through MLCK activation, consistent with the previous finding that higher aspect ratio VSMC are more contractile[47, 48]. To our knowledge, this is the first demonstration of a direct relationship between cell shape, Ca^{2+} signaling and contractility. The differences in nuclear Ca^{2+} between circle and elliptical cells were distinct from cytoplasmic Ca^{2+} (Fig. 4h). In the nuclear region, the peak Ca^{2+} amplitudes of circle and elliptical cells were similar. However, there is a notable delay in the rate of nuclear Ca^{2+} increase to maximum in elliptical cells compared to circular cells, but the decay times in elliptical cells were slower as well, resulting in a significantly higher temporally integrated Ca^{2+} in elliptical cells compared to circular cells (Fig. 4i). These results indicate that cell shape affects nuclear

Ca^{2+} transients mediated by M_3R/PLCβ and elliptical cells is more prolonged, resulting in higher integrated Ca^{2+} compared to circular cells. Increase in nuclear Ca^{2+} in elliptical cells is likely to impact the nucleo-cytoplasmic transport of NFAT, which exhibits a Ca^{2+}/calcineurin dependent translocation to the nucleus[18, 49]. We measured NFAT-GFP localization dynamics in live VSMCs in elliptical and circular micropatterns in response to $G\alpha_q$ activation through M_3R stimulation (Fig. 4j-m). Elliptical cells exhibited greater NFAT-GFP nuclear localization compared to circular cells (Fig. 4k) and on average displayed higher maximal $NFAT_{nuc/cyto}$ (Fig. 4l). We further validated the differences in NFAT translocation by immunofluorescence of NFAT1 (Fig. 4m, Supplementary Fig. 10a). At basal levels, $NFAT_{nuc/cyto}$ were similar between circular and elliptical cells. However, elliptical cells displayed higher nuclear NFAT compared to circular cells at 30 minutes and 1 hour after stimulation, consistent with live-cell NFAT-GFP translocation results. We asked the question whether other Ca^{2+} dependent transcription factors are also impacted by shape. Ca^{2+} also triggers the nuclear localization of SRF through nuclear Ca^{2+}/CaMKIV[19] and Rho/ROCK/actin dynamics[50, 51]. Elliptical VSMC show increased nuclear SRF compared to circular cells at both basal and stimulated levels (Supplementary Fig. 10b). In contrast there was no difference in myocardin intensity or translocation dynamics between circle and elliptical cells (Supplementary Fig. 10c) suggesting that myocardin is constitutively active[20, 52]. Taken together, these results indicate that shape-induced modulation of Ca^{2+} signaling alters the activities of Ca^{2+} dependent transcription factors.

An integrated model of shape and organelle location provides insight into curvature coupling of Ca^{2+} dynamics in VSMCs.

Our previous models were focused on localized PM-SR interactions in highly idealized geometries (Fig. 3). However, ultrastructural analyses have shown that the ER is a highly dynamic, tubular network that occupies roughly 10% of the cytosolic volume and extends from the nucleus to the cell periphery[53]. We developed an integrated whole cell, multi-compartmental partial differential equation model in *Virtual Cell* to derive relationships between experimental observations and models at the whole cell level (Fig. 5a-l). Upon stimulation of M_3R, the concentration gradients of IP_3 and cytoplasmic Ca^{2+} were highest in regions where PM-SR distance was lowest (cell body), and lowest in regions where PM-SR were farthest from each other (cell tips) (Fig. 5a and Fig. 5c), establishing an IP_3 and Ca^{2+} gradient from the cell body to the tips which progressively became steeper with aspect ratio. More importantly, increasing the AR increased global IP_3 and Ca^{2+} levels in both cytoplasmic and nuclear compartments (Fig. 5b, Fig. 5d-h). Hence, elliptical cells are predicted to exhibit increased global cytoplasmic and nuclear Ca^{2+} compared to circular cells upon stimulation of M_3R due to decreased PM-SR and PM-nuclear distance in the short axis of the cell. This model failed to capture the delay in the rate of nuclear Ca^{2+} increase to maximum in elliptical cells (Fig. 4h). This suggest that the model specification was incomplete and additional details may be needed to make the model more realistic[54]. Since cell shape determines nuclear shape, we hypothesized that as the cell elongates, invaginations in the nuclear membrane may decrease. As nuclear invaginations have been shown to be related to nuclear calcium dynamics[55-57], we introduced a calcium permeability term in the model, by introducing a second order reaction dependent on the nuclear permeability, NPC, using the same circle and elliptical geometries (Supplementary Fig. 12). NPC represents the net nuclear permeability which may be due to an increase in nuclear membrane surface area and/or increase in nuclear pores; if NPC=0, the nuclear membrane is completely impermeable to cytoplasmic Ca^{2+}; if NPC=1, the nuclear membrane is completely permeable to the cytoplasmic

Ca^{2+} and mirrors the cytoplasmic Ca^{2+} transient. When nuclear permeability in circular cells was three times higher compared to elliptical cells, there was closer agreement between the model and experimental temporal behavior in both cytoplasmic and nuclear Ca^{2+} (Fig. 5i-l), suggesting that nuclear membrane of elliptical cells are less permeable to cytoplasmic Ca^{2+}, compared to circular cells. The net effect of decreased nuclear permeability led to higher integrated nuclear Ca^{2+} signals in cells, which increases its availability for slower downstream processes in the nucleus that are driven by Ca^{2+} [25, 26]. Thus the whole-cell model, coupled with organelle location based on curvature, captures key findings of Ca^{2+} dynamics in VSMC of different shapes.

DISCUSSION

One of the key features of signal transduction is the spatial organization of information propagation. Here, we bring together several seemingly independent effects due to change in global cell shape to provide an integrated view of how curvature, affects organelle location as well as distribution of receptors in the plane of the membrane to modulate signal transduction and thus affect cellular function (Fig. 6). Shape and biochemical signaling are coupled together in a feedback loop to maintain phenotype: cell shape integrates external mechanical and chemical signals on the plasma membrane[3, 4] while intracellular signaling cascades containing chemical information in the form of reaction kinetics, in turn regulate cell shape[58, 59]. We propose that shape-dependent endomembrane and nuclear organization serves as the critical link that connect these two components in the feedback loop. This intricate, non-linear coupling of geometric and chemical information can potentially lead to signal amplification to control phenotype.

We used VSMC as a model system to unravel the complex relationship between global cell curvature, signaling, and endomembrane organization. During atherogenesis, disruption of local microenvironment in the medial layer of blood vessels causes VSMC to lose its native spindle shape, and subsequently lose contractile function[24, 60]. It was not clear how loss of shape can to a decrease in contractile function. This study provides a mechanistic explanation for the functional role of shape in VSMC contractile function. Cell shape governs membrane curvature, which enables the emergence of systems level properties; cell elongation simultaneously concentrates plasma membrane receptors in the flatter regions of the membrane and reduces the distance between the PM-SR and SR-nucleus in the same region, hence effectively forming a diffusion-restricted domain where receptors, SR and the nucleus become closer to each other, establishing high effective IP_3 and Ca^{2+} concentration in the cell center. Given the slow diffusion coefficient of IP_3 ($\leq$ 10 $\mu m^2/s$) which limits the range of action over which it can exert its signal[61] and the dimensions of typical spindle-shaped VSMC (long axis $\geq$150 µm and short axis length of $\leq$ 10 µm), control of endomembrane organization by cell shape is a physical, non-genomic mechanism by which IP_3/Ca^{2+} signals can be locally amplified in order to achieve high concentration of Ca^{2+} globally. These can further regulate contractility and Ca^{2+}-dependent gene expression in the nucleus. Although the effect of cell shape on individual readouts of signaling may appear small, the collective and progressive amplification of signal transduction through coupled reaction kinetics and spatial organelle organization is sufficient to result in different regimes of phenotypic function.

While we have extensively explored the role of cell shape in signaling here and previously[3, 4], features that we have not considered here, such as the forces exerted by the extracellular

microenvironment on the cell, and vice versa, also play a critical role in transmitting geometric information[62, 63], trafficking[64], and signal transduction[65]. Furthermore, the interaction between signaling and cytoskeletal remodeling can lead to changes in cell shape and local curvature[66, 67]. Our observations of increasing anisotropy and robustness in expression of actin myofibrils, along with increased nuclear SRF localization with aspect ratio indicate that cytoskeletal signaling also contributes towards the contractile phenotype of VSMC. Cytoskeletal and Ca^{2+} signaling may act in concert in maintaining the differentiated phenotype of spindle-shaped VSMC. We were able to uncover unique aspects of signal flow in cells based on geometry and chemical reaction cascades alone and coupling the role of cytoskeletal interactions is a focus of future studies. We conclude that being at the right place at the right time is critical for information to flow from one compartment to another and for short term signals like Ca^{2+} to have long lasting effects such as contractility and transcription factor activity. Like real estate, it seems that cells have the same motto – location, location, location!

METHODS

Cell culture. A10 cells, which are VSMC from thoracic/medial layer of rat aortas, were obtained from American Type Culture Collection (CRL-1476). A10 cells were maintained in Dulbecco's modified eagle's medium (DMEM, Gibco), supplemented with 10% Fetal Bovine Serum, 1% penicillin/streptomycin, at 37 °C and 5% CO_2. Cells were transfected using Neon Transfection System (Life Technologies) according to manufacturer's instructions. Briefly, 5 x 10^5 cells were electroporated with 1 µg DNA in suspension buffer, with the following electroporation settings: 1400 V, 2 pulses, 20 ms pulses each. Cells were then suspended in DMEM supplemented with 10% FBS and then allowed to adhere on micropatterned surfaces. Forty-eight hours post-transfection, cells were imaged using Hanks Balanced Salt Solution (HBSS) supplemented with $CaCl_2$, $MgCl_2$ and 10 mM HEPES.

Micropatterning. Patterned surfaces were fabricated by conventional photolithography using SU8 photoresist[68]. Briefly, cover glass slides were cleaned by sonication in isopropanol and deionized water for 15 minutes and baked at 110 °C overnight and photolithography was subsequently performed using standard vacuum hard-contact mode. Before plating of cells onto micropatterns, microfabricated surfaces were washed with 50 µg/mL gentamicin and then incubated with 0.5% Pluronic for at least 3 hours. Micropatterns were then washed with PBS and were seeded with cells.

Immunofluorescence of cells in micropatterns. Cells were seeded onto the micropatterned coverslips and were allowed to adhere and comply with the patterns for at least 24 hours. After assay treatments, cells were fixed with 4% paraformaldehyde (Electron Microscopy) for 15 minutes at room temperature, washed with PBS, permeabilized with 0.2% saponin for 30 minutes and blocked with 4% normal goat serum doped with 0.05% saponin for 1 hour. Cells were then incubated overnight with primary antibodies (sources and catalog numbers shown in table below) that had been diluted in blocking solution at 4 °C. Cells were washed with PBS and samples were incubated with secondary antibodies (Alexa 488, Alexa 568 and/or Alexa 647) for 1 hour at room temperature. For organelle staining, cells were counter-stained with Actin Green and DAPI counterstains in addition to the secondary antibodies. Cells were then imaged on a Zeiss LSM 880 microscope equipped with 60x objective. Same acquisition settings were applied across different conditions that were compared (laser power, gain settings, magnification, zoom, pixel size and slice thickness). For quantitative immunofluorescence of M_3R, a Z-stack of 30-40 slices using a slice thickness of 0.5 µm were obtained for each cell. Z-stack datasets were then pared down to 21-22 slices encompassing the entire height of the cell (mean cell height ~ 10 µm). Alignment, registration and cropping were performed to ensure each image had the same x-y dimensions (circular cells = 253 x 246 pixels, elliptical cells (AR 1:10) = 106 x 512 pixels). Per condition, images of cells obtained from the same z-plane (3.0 µm from the confocal slice corresponding to the bottom region of the plasma membrane), were averaged to obtain the averaged distribution of M_3R in different regions of the cell. For immunofluorescence of transcription factors, multi-channel images consisting of DAPI, Actin Green (Invitrogen), and primary antibodies for NFAT, SRF or myocardin were aligned and stitched using the ZEN 2014 software. Image analysis and quantification was performed using ImageJ scripts. Briefly, nuclei were segmented in the DAPI channel. Corresponding cytosol and whole cell objects were outlined utilizing the contrast enhanced phalloidin channel to define cell boundaries. Nuclear-to-cytoplasmic transcription factor ratio was defined as the ratio of the mean transcription factor

intensity colocalizing with the nuclear object divided by the mean intensity of the corresponding cytosol object. All measurements were exported directly to csv files and were subsequently analyzed using MATLAB to generate plots.

Antibody	Dilution	Source
Calnexin	IF 1:100	Abcam, cat # ab22595
Protein Disulfide Isomerase (PDI) (C81H6)	IF 1:100	Cell Signaling, cat # 3501
Nogo-A/Reticulon-4	IF 1:100	Cell Signaling, cat # ab47085
α-tubulin	IF 1:100	Cell Signaling, cat # 2144
AIF mitochondrial marker (D39D2)	IF 1:100	Cell Signaling, cat # 5318
EEA1 – Early endosome marker (C45B10)	IF 1:100	Cell Signaling, cat # 3288
RCAS1 (D2B6N) Golgi marker	IF 1:100	Cell Signaling, cat # 9091
Muscarinic Acetylcholine Receptor 3 (M_3R)	IF 1:100	Abcam, cat # ab126168
NFATc1 antibody	IF 1:100	Abcam, cat # ab2722
SRF antibody	IF 1:100	Cell Signaling, cat # 4261
Myocardin	IF 1:100	Abcam, cat # 22073

Airy-scan Imaging of Live Cells. VSMC conforming in micropattern were simultaneously labeled with 1 µM CellMask Plasma Membrane tracker (Life Technologies), 1 µM CellMask ER marker (BODIPY TR Glibenclamide), in HBSS buffer supplemented with 1% Pyruvate, 1% HEPES and 1 mM Trolox, for 5 minutes at room temperature. Images were acquired using Zeiss LSM 880 using Airy-scan imaging equipped with 63x 1.4 Plan-Apochromat Oil objective lens at 30 ºC. Z-stacks using with an interval of 0.15 µm were collected for the entire cell height which approximated 10-12 µm. Z-stack analyses and other post-acquisition processing were performed on ZEN software (Carl Zeiss).

Calcium Measurements. VSMC were seeded on micropattern coverslips. Calcium measurements in micropatterns were performed as previously described with modifications[69]. Briefly, cells in micropatterns were serum-starved for 12 hours and loaded with 5 µM of calcium green (dissolved in DMSO) for 30 minutes at room temperature, with Hanks Balanced Salt solution, (HBSS) supplemented with $CaCl_2$, $MgCl_2$ and 10 mM HEPES. Calcium Green was imaged using Zeiss 510 equipped with 40x Apochromat objective at acquisition frame rate of 4 fps (250 ms acquisition time), and Calcium Green was excited using Argon ion laser 488 at low transmittivity (1%) to prevent photobleaching. Image stacks acquired were then imported into Fiji/ImageJ. Background subtraction were performed on the time stacks by using a rolling ball radius of 50 pixels. Cytoplasm and nuclear regions of interest (ROI) were chosen by performing a maximum intensity projection of the time-stack and specifying a 5 µm radius circle within the the nuclear and cytoplasmic regions. To convert intensity values to Ca^{2+} concentration, modified Grynkiewicz equation was used, defined as: [Calcium] = $K_D[\frac{(F-Fmin)}{(Fmax-F)}]$. Where F_{min} is the average fluorescence intensity of the ROI after addition of 100 µM BAPTA AM, F_{max} is the average fluorescence intensity of the ROI after addition of 0.100 µM A23187. Integrated Ca^{2+} were obtained using the trapz() function in MATLAB.

FRET imaging. MLCK-FRET plasmid is a kind gift from Dr. James T. Stull (University of Texas Southwestern Medical Center). The MLCK-FRET plasmid is a calmodulin-binding based sensor where calmodulin binding sequence is flanked with eCFP and eYFP and exhibits decreased FRET upon binding with calmodulin[46,18]. Cells expressing MLCK-FRET were imaged

using Zeiss LSM 880 (Carl Zeiss, Jena, Germany), at 37 ºC incubator, fitted with Plan-Apochromat 20x, equipped with 458 nm and 514 nm Argon ion laser lines for excitation of eCFP and eYFP respectively. Incident excitation light was split using an MBS 458 nm/514 nm beam splitter and collected on a 32-spectral array GaAsp detector. The fluorescence emission was collected from 463-520 nm (ECFP), 544-620 nm (FRET channel and eYFP channel). Intensity based ratiometric FRET were obtained using custom-written scripts in ImageJ and MATLAB. Since MLCK-FRET is a single-chain construct, decrease in FRET, and increase in MLCK binding to calmodulin, was expressed as the ratio of emission intensity at 520 nm/emission intensity at 510 nm normalized at the basal levels.

NFAT imaging. HA-NFAT1(4-460)-GFP was a gift from Anjana Rao (Addgene plasmid # 11107). Patterned cells expressing NFAT-GFP was imaged using Zeiss 880, using Argon ion laser 488 nm, as described above and 1.4 NA objective, with an acquisition rate of 1 frame every 10 seconds. Time series image stacks were analyzed using ImageJ. Regions of interest of identical size were drawn in the cytoplasmic and nuclear regions of interest and the ratios of these intensities were computed over time.

Electron Microscopy. Micropatterned coverslips containing fixed A10 cells were embedded in Embed 812 resin (Electron Microscopy Sciences (EMS), Hatfield, PA) using the following protocol. Cells were rinsed in 200mM phosphate buffer (PB), osmicated with 1% osmium tetroxide/PB, washed with distilled water (dH20), and *en bloc* stained with aqueous 2% uranyl acetate, washed with dH2O and dehydrated via increasing ethanol (ETOH) series /distilled water (25%, 60%, 75%, 95% and 100% ETOH). Cells were further dehydrated using propylene oxide (PO), and embedded using ascending PO:EPON resin concentrations (2:1, 1:1, 1:2, pure). Prior to solidification, the coverslips were placed on 1”X 3” microscope slides, and multiple open ended embedding capsule with a 1 × 1 cm face (EMS) were placed on the coverslips covering the areas of interest. The resin was then polymerized in a vacuum oven at of 65 °C for 8–12 hours. After the first layer was solidified, the capsule was topped off with more resin and put back in the oven for another 8–12 hours. Capsules containing micropatterned cells were removed from coverslips using previously described methods[70]. Briefly, to separate the block from the coverslip, a hot plate was heated to 60°C and the microscope slide was placed directly on a pre-heated hot plate for exactly 3 minutes and 30 seconds. The slide was removed from the hot plate and the capsules carefully dislodged free from the coverslips. Once separated, the block face retains the cells within the micropatterns. The block was coarsely trimmed with a double-edged razorblade, and a Diatome cryotrim 45° mesa-trimming knife (EMS) was used to finely trim the block. Using as large a block face as possible, 70 nm ultrathin sections were cut from the block surface using an ultra-thin diamond knife (EMS), and a Leica EM UC7 ultramicrotome (Buffalo Grove, IL). All sections coming off the block face were collected. Sections were collected using a Perfect Loop (EMS) and transferred to a 2 × 1 mm formvar-carbon coated reinforced slot grid (EMS). The sample was dried on the grid and transferred to Hiraoka Staining Mats (EMS) for heavy metal staining. Grids were stained with 3% uranyl acetate in water for 40 minutes, washed and stained with Reynold’s lead citrate for 3 minutes, washed and allowed to dry. Electron microscopy images were taken using a Hitachi 7000 Electron Microscope (Hitachi High Technologies America, Inc.) equipped with an AMT Advantage CCD camera. Cells were viewed at low-magnification to identify areas of interest (cell tip versus cell body) before high magnification imaging. Images were transferred to Adobe Photoshop CS3 (version 10), and adjusted for brightness and contrast. Measurement of plasma membrane to ER distances from

electron microscopy images were performed blindly. Briefly, sample information from images were removed and images were saved with a randomized filename. Image contrast was further enhanced using ImageJ using contrast-limited adaptive histogram equalization (CLAHE). Only images with discernible smooth ER closely apposed to the plasma membrane were analyzed and distances were measured at optimal xy orientations at 50 nm intervals using ImageJ. Data was graphed using Excel and MATLAB.

Statistics. Results are presented as mean $\pm$ standard error of the mean from at least three independent experiments. Normality was determined using Shapiro-Wilk test using a p-value $\geq$ 0.05. If distribution is normal, a two-tailed Student's t-test was performed. For datasets with non-normal distribution, two-tailed Mann-Whitney test was used. $P < 0.05$ was considered statistically significant.

Model Development. We formulated a phenomenological model to study the role of PM-SR distances. The complete derivation and mathematical solution is given in the supplementary material. Complete details of the simulations using finite-element methods in COMSOL and using finite-volume methods in *Virtual Cell* are given in the Supplementary Material.

ACKNOWLEDGEMENTS

We thank Dr. Eric Sobie, Dr. Marc Birtwistle and Dr. Evren Azeloglu for discussion and reagents. This work was supported NIH Grants GM072853 and the Systems Biology Center grant P50GM071558. RC was supported by a NIH postdoctoral fellowship F32GM116415 and research in PR's laboratory is supported by ARO W911NF-16-1-0411, AFOSR FA9550-15-1-0124, and NSF PHY-1505017.

FIGURE 1

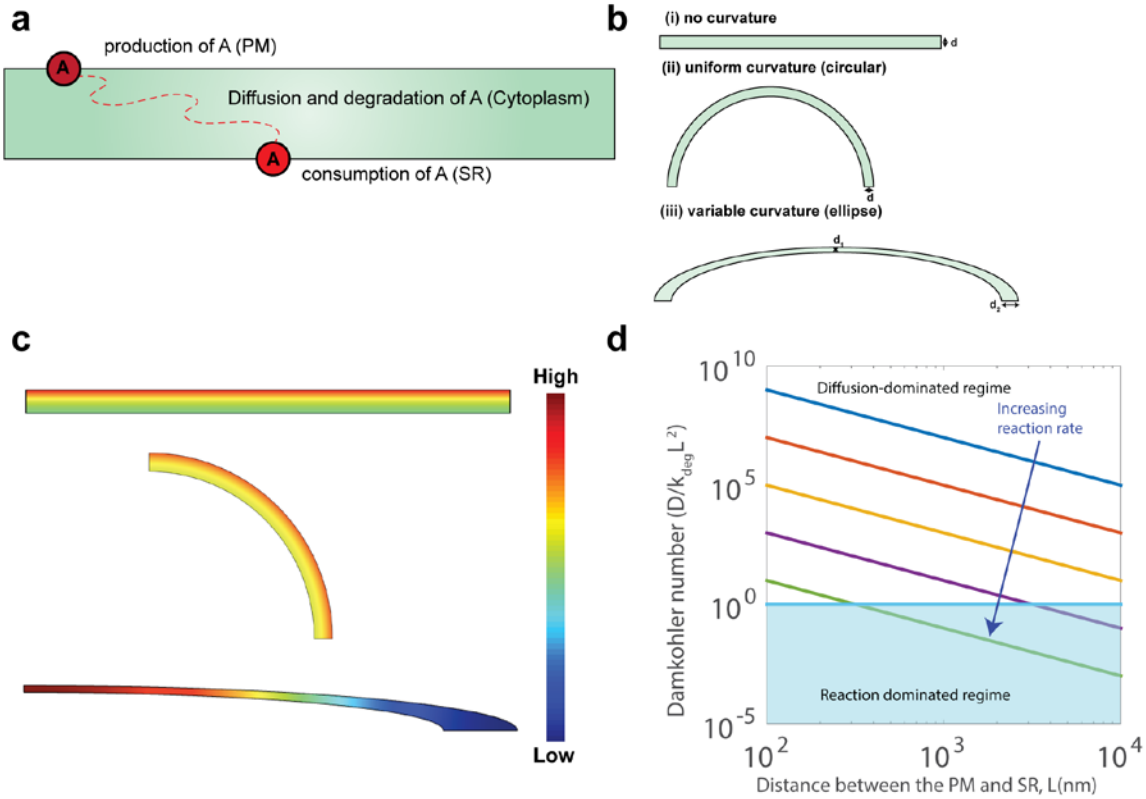

Figure 1 Phenomenological model describing the dynamics of a signaling molecule produced at a membrane and consumed at a neighboring membrane compartment as a function of curvature. (a) Dynamics of a signaling molecule can be described by its production, diffusion, and degradation in the cytoplasmic space and consumption at a neighboring membrane. (b) Three different geometries were used to test how curvature and distance between PM and SR affect the spatio-temporal dynamics of A. (c) Reaction-diffusion modeling predicts that curvature and distance between the PM and SR will both affect the spatial distribution of A. (d) The Damkohler number for different values of PM-SR distance, d, and rate of degradation. For physiological distances, the dynamics of A are diffusion dominated.

FIGURE 2

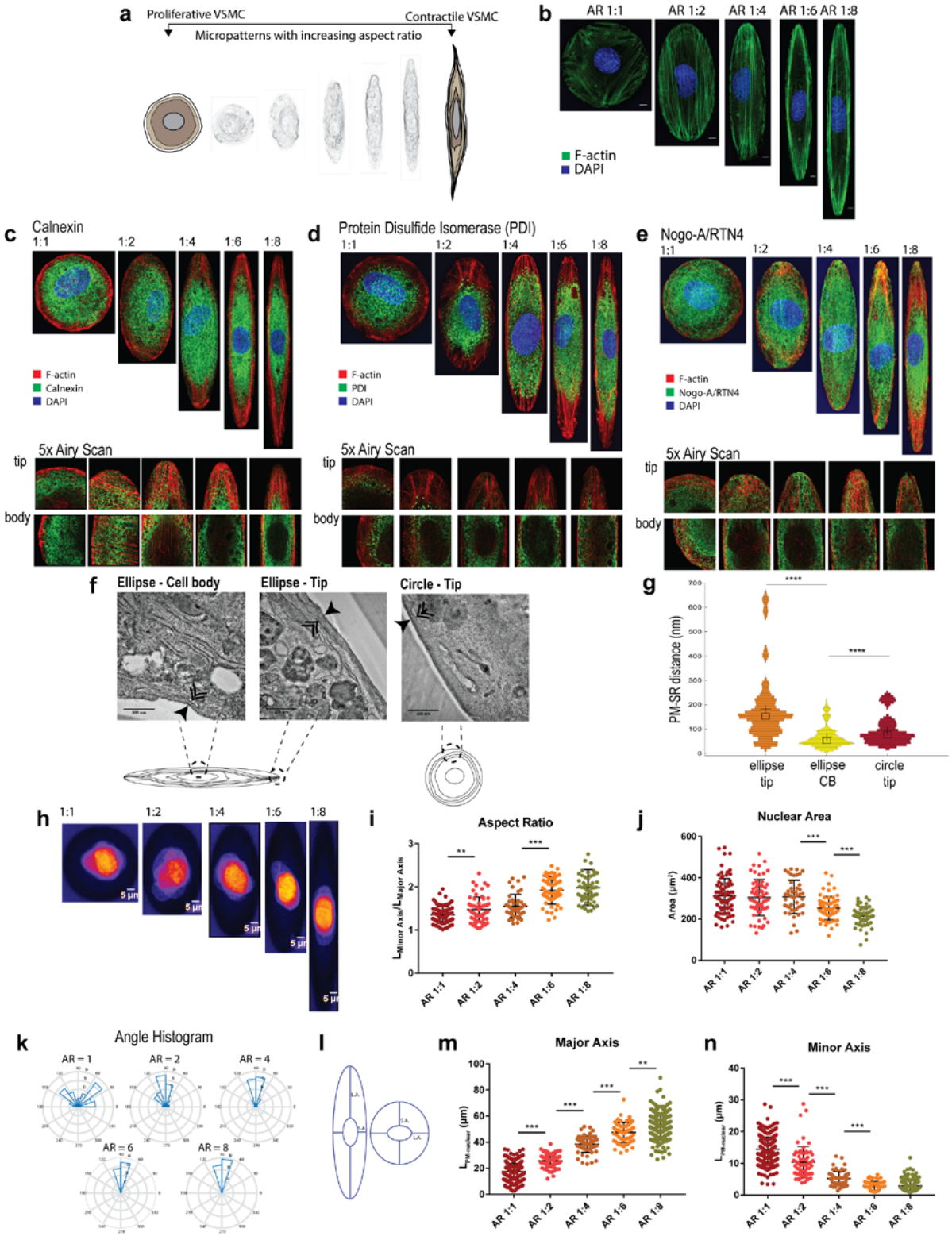
a
Proliferative VSMC
Contractile VSMC
Micropatterns with increasing aspect ratio
b
AR 1:1
AR 1:2
AR 1:4
AR 1:6
AR 1:8
F-actin
DAPI
c
Calnexin
1:1
1:2
1:4
1:6
1:8
F-actin
Calnexin
DAPI
5x Airy Scan
tip
body
d
Protein Disulfide Isomerase (PDI)
F-actin
PDI
DAPI
e
Nogo-A/RTN4
F-actin
Nogo-A/RTN4
DAPI
f
Ellipse - Cell body
Ellipse - Tip
Circle - Tip
g
PM-SR distance (nm)
ellipse tip
ellipse CB
circle tip
h
5 µm
i
Aspect Ratio
AR 1:1
AR 1:2
AR 1:4
AR 1:6
AR 1:8
j
Nuclear Area
Area (µm²)
k
Angle Histogram
AR = 1
AR = 2
AR = 4
AR = 6
AR = 8
l
m
Major Axis
n
Minor Axis

Figure 2 Shape impacts cytoskeletal organization and organelle location. Whole cell shape changes location and distribution of subcellular organelles in a systematic manner. (a) Biomimetic, microfabricated surfaces with graded aspect ratios fine-tune the shape of VSMC and its enclosed organelles. (b) Actin organization is dependent on cell shape (scalebar, 10 µm). (c-e) SR distribution in VSMC seeded in AR 1:1 to 1:8 staining for SR membrane markers (panels below show 5x magnified Airy scan images of tip and body of images shown) (c) calnexin (d) protein disulfide isomerase (PDI) and (e) reticulon-4 (f) Representative TEM micrographs sampled from corresponding regions in micropatterned cells (cartoon). Single-headed arrows indicate the plasma membrane and double-arrrows indicate smooth, peripheral SR, apposed to the plasma membrane (scalebar, 500 nm). (g) Distribution plots of PM-SR distances obtained from TEM images, mean and median are shown as crosses and squares respectively ($N_{ellipse\ tip}$=329, $N_{cell\ body}$ = 254, $N_{circle\ tip}$ = 115, ****P $\leq$ 0.0001, two-tailed Mann-Whitney test). (h) Cell shape affects nuclear shape size and distance to PM. Representative images of VSMC compliant in patterns with increasing AR stained for DAPI. Scatterplots of whole aspect ratio versus (i) nuclear aspect ratio (j) size (area, µm^2) (k) orientation with respect to the major axis of the cell. (l) Distances between nuclear and plasma membrane boundaries were measured along the long and short axes of the nucleus. (m) Increasing the cellular aspect ratio increases the distance between the nucleus and the plasma membrane in the major axis of the cell while (n) decreasing the PM-nuclear distance in the minor axis of the cell ($N_{AR1:1}=82$, $N_{AR1:2}=60$, $N_{AR1:4}=45$, $N_{AR1:6}=65$, $N_{AR1:8}=54$, **P $\leq$ 0.05, ***P $\leq$ 0.0001, two-tailed t-test).

FIGURE 3

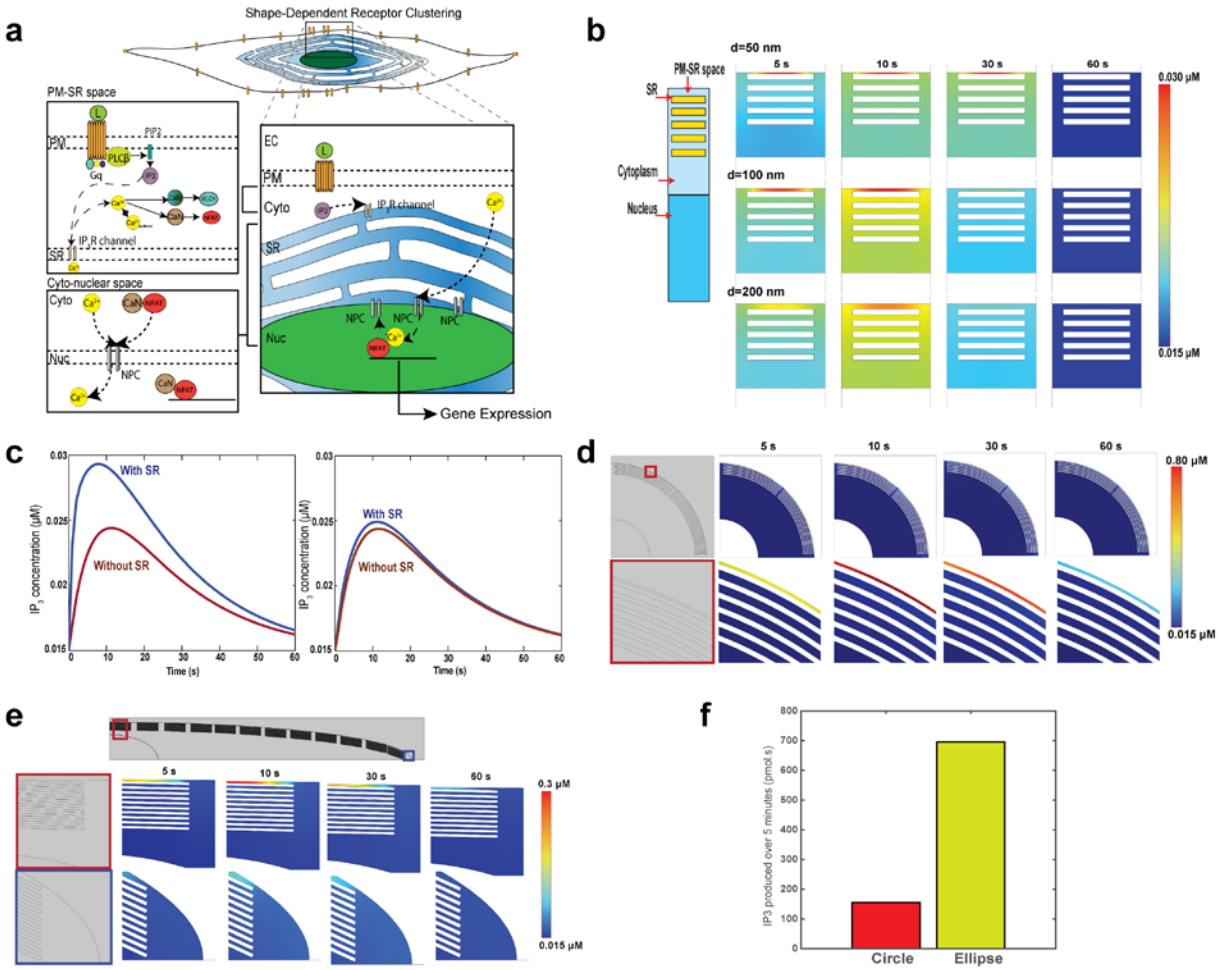

Figure 3. Small length scale simulations show critical relationship between IP3 signaling and distance. Biopsy-punch simulations show the dependence of IP_3 dynamics on PM-SR distance. (a) Biochemical events which govern Ca^{2+} signaling in VSMC including GPCR-$G_{\alpha q}$ cycling on the membrane, PLC_β activation, IP_3 production and IP_3R-mediated Ca^{2+} release from SR. (b) IP_3 concentration at geometries with varying PM-SR distances, from 50 nm to 200 nm. (c-d) Temporal dynamics of IP_3 in locations with and without SR for different PM-SR distances of (c) 50 nm (d) and 500 nm. (e) IP_3 concentrations in circular geometry (f) IP_3 concentrations in elliptical geometries. (g) IP_3 concentration over space (the entire domain) and time were integrated, since integration of signal over time provides a buffer for time scale and damps out the effect of temporal fluctuations[71] and spatial integration allows for conversion from concentration (moles per unit volume) to amount (moles). Shown are graphs comparing integrated IP_3 in circular and elliptical geometries.

FIGURE 4

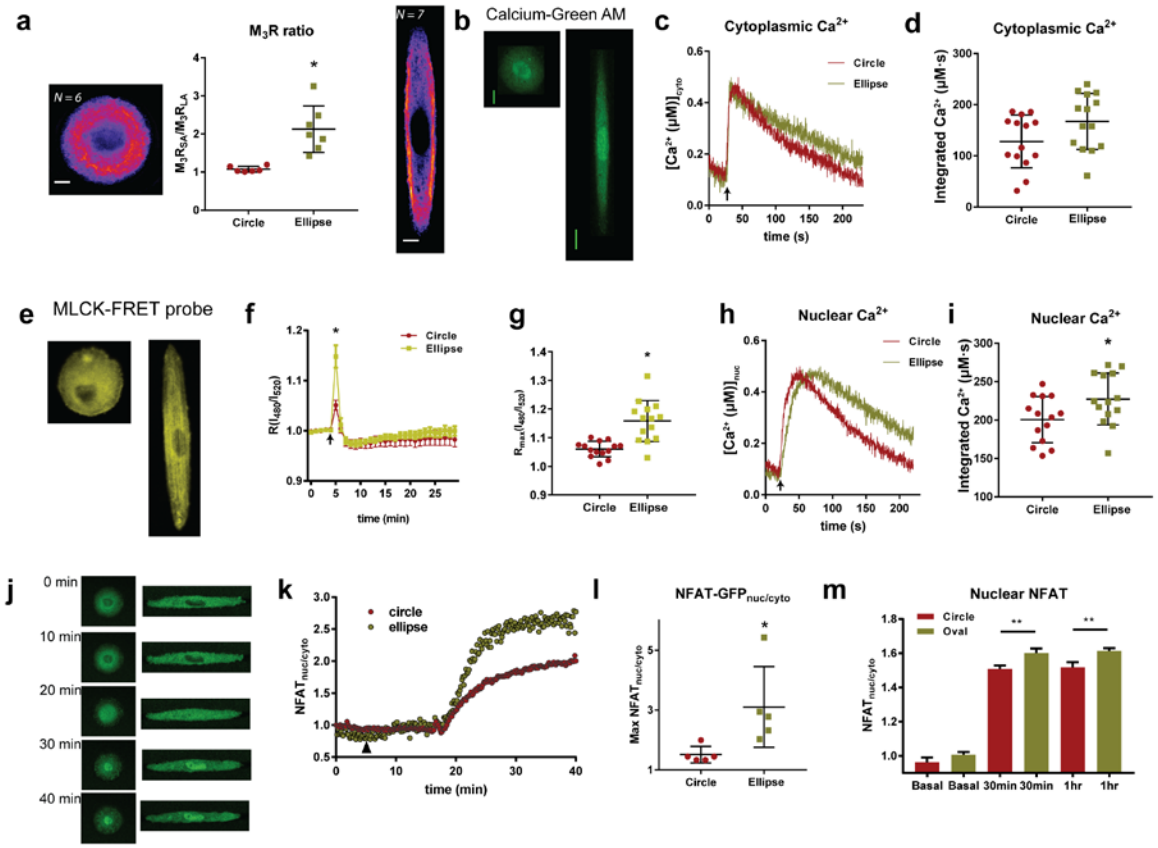

Figure 4. Shape impacts $M_3R/IP_3/Ca^{2+}$/NFAT signaling in VSMC. (a) Average intensity of M_3R along the length of the cell in circular (*N=6)* and oval *(N=7)* VSMC. Differences in anisotropic distribution of M_3R were quantified by obtaining the ratio of M_3R staining intensities on the short and long axes (M_3R_{SA}/M_3R_{LA}, mean$\pm$SEM ellipse=2.1 $\pm$ 0.6 A.U. *N = 7*, circle= 1.1 $\pm$ 0.1 A.U., *N=6*, *P=0.0016, two-tailed t-test). (b) Circular and elliptical cells were loaded with Calcium-Green AM dye, to measure Ca^{2+} signaling in response to 10 μM carbachol (c) average time-course of cytoplasmic Ca^{2+} in response to CCh (circle, N=14, oval, N=14, stimulated at arrow indicated) (d) Scatterplot of cytoplasmic integrated Ca^{2+} (area-under-the-curve) per cell in circular and elliptical cells. (e) Circle and elliptical cells expressing MLCK-FRET probe (f) temporal MLCK activation in circular and ellipse VSMC upon stimulation with carbachol, activation was measured by decrease in FRET and increase in R480/520 (g) scatterplot of maximal $R(I_{480}/I_{520})$ from individual cells expressing MLCK-FRET probe. (*P$\leq$0.0001, two-tailed Mann Whitney test). (h) average time-course of nuclear Ca^{2+} in response to CCh (i) scatterplot of nuclear integrated Ca^{2+} (area-under-the-curve) in circular and elliptical VSMC. (*P = 0.035, two-tailed t-test).(j) Representative VSMC complying to circle and elliptical micropatterns expressing NFAT-GFP, in basal and after stimulation with carbachol (k) Representative NFAT-GFP time-course (l) scatterplot of maximal $NFAT_{nuc/cyt}$ ratio in circle and elliptical cells Max $NFAT^{circle}_{nuc/cyto}$=1.51$\pm$0.12, *N=5*, Max $NFAT^{ellipse}_{nuc/cyto}$=3.10$\pm$0.60, *N=5*, p-value=0.0325, two-tailed t-test (*P = 0.0325, two-tailed t-test, N=5 for each group). (m) Quantification of endogenous NFAT translocation ($NFAT_{nuc/cyt}$) in basal and M_3R stimulated states, in circle and ellipse VSMC. Shown are mean$\pm$SEM, (at time = 30 minutes, **P = 0.024, at time = 1 hour, **P = 0.010, two-tailed Mann-Whitney test).

FIGURE 5

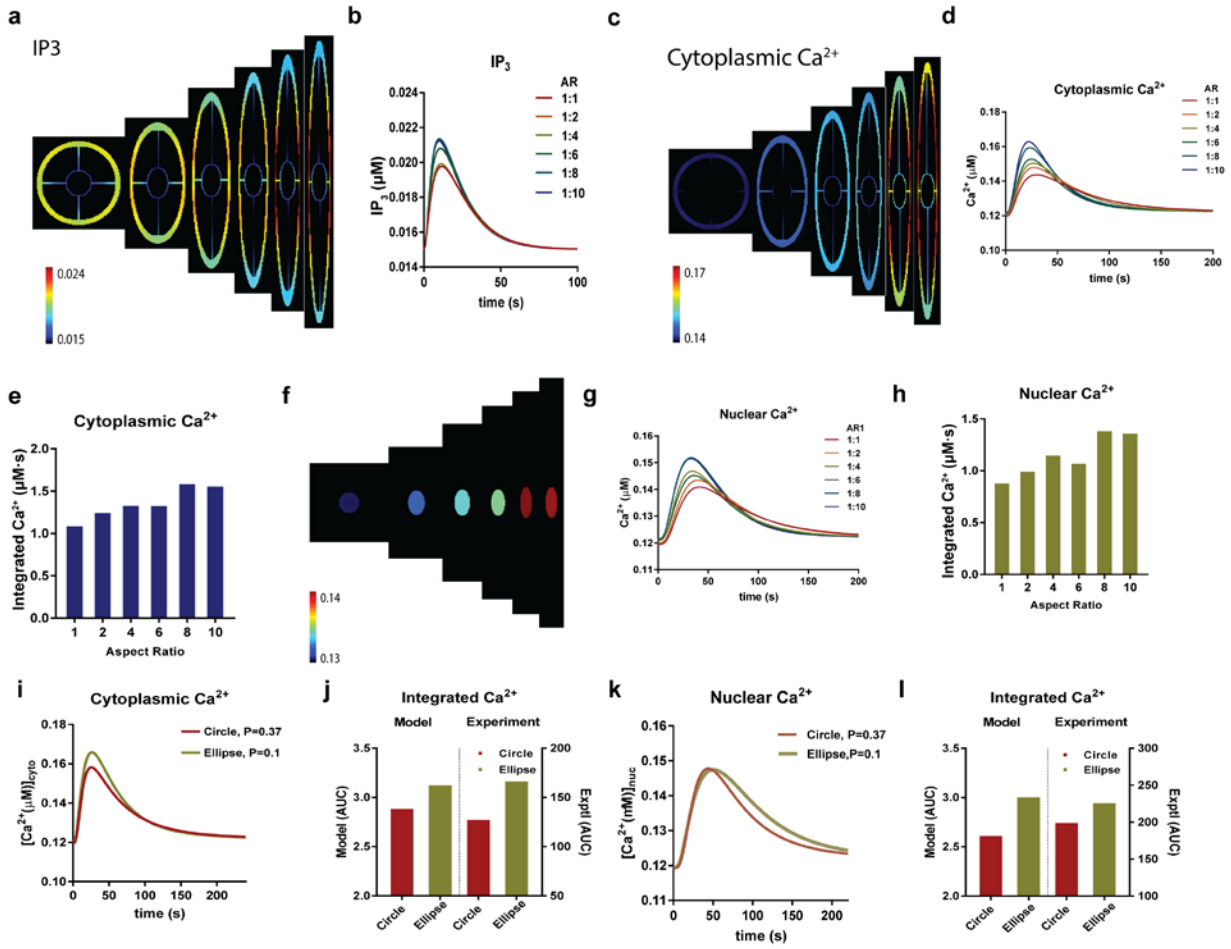

Figure 5. Whole-cell spatial models provide mechanistic understanding of cell elongation - induced Ca^{2+} potentiation. Whole-cell simulations show the effect of cell elongation on inter-organelle distances on IP_3/Ca^{2+} potentiation. Whole cell, spatio-temporal PDE model of IP_3 and Ca^{2+} using *VCell.* (a) Global IP_3 gradients exhibit progressively steeper gradients with increasing cell aspect ratio, with the highest concentration in the flatter regions of the cell (cell body) (b) IP_3 temporal dynamics in increasing cell aspect ratio (c). The relationship between IP_3 and cell aspect ratio is preserved downstream, on cytoplasmic Ca^{2+} gradients (d) and temporal Ca^{2+} dynamics in varying aspect ratios (e) Integrated Ca^{2+} (AUC) (f-h) Nuclear Ca^{2+} spatio-temporal models predict that higher cell aspect ratio increase integrated Ca^{2+} in both cytoplasmic and nuclear compartments. Nuclear compartment of the whole cell model was modified to account for nuclear permeability due to nuclear shape. (i-l) Modified model demonstrates delayed rise to maximal in elliptical cells due to decreased nuclear permeability (circle, P = 0.37, elliptical = 0.1). Bar plot panels next to time course show agreement of spatio- temporal model with experiment.

FIGURE 6

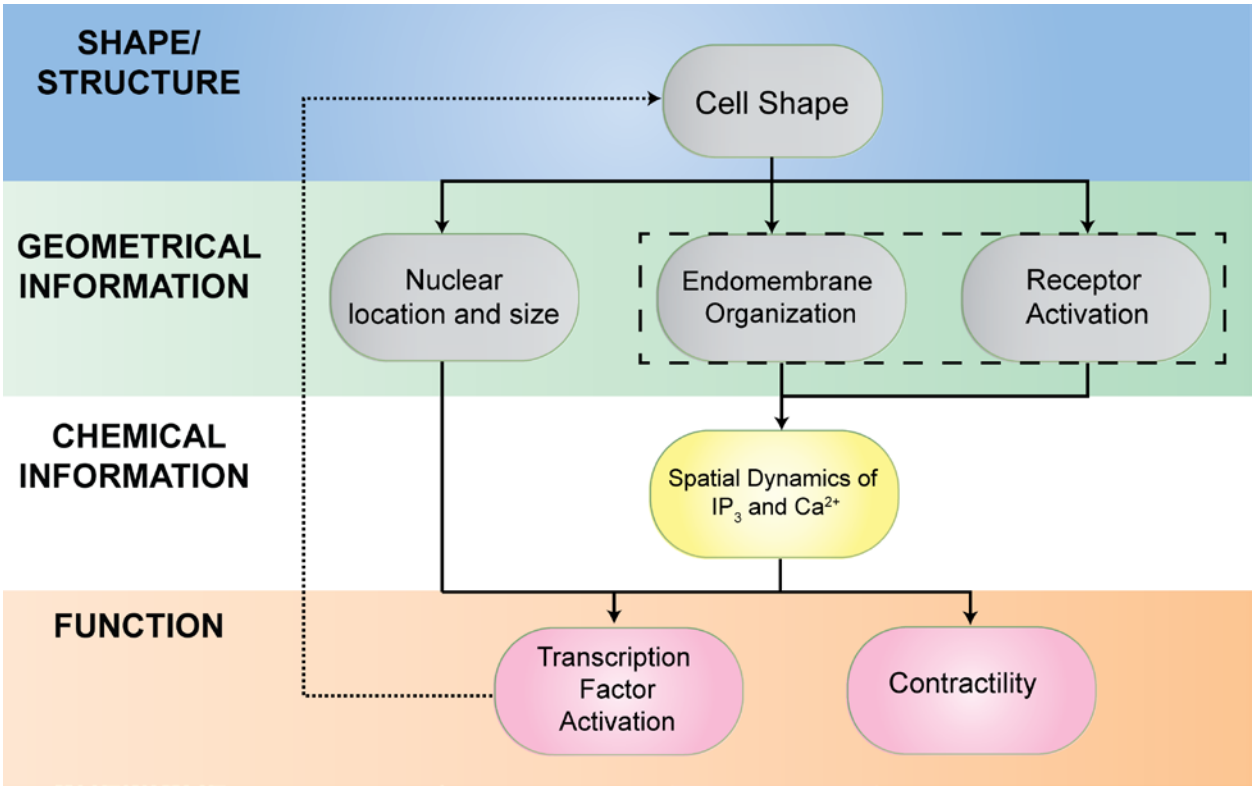

Figure 6. Systems Approaches to controlling signaling through subcellular organization hierarchy. Physical determinants such as shape and geometrical information within the cell interact with organelle location and chemical information transfer to impact cellular function and gene expression, which in turn, feedback into cell shape. While each of these effects – shape, organelle location and chemical information – may separately lead to small changes in signaling, collectively, these effects can lead to altered cellular function including transcription factor activation and contractility.

SUPPLEMENTARY FIGURE 1

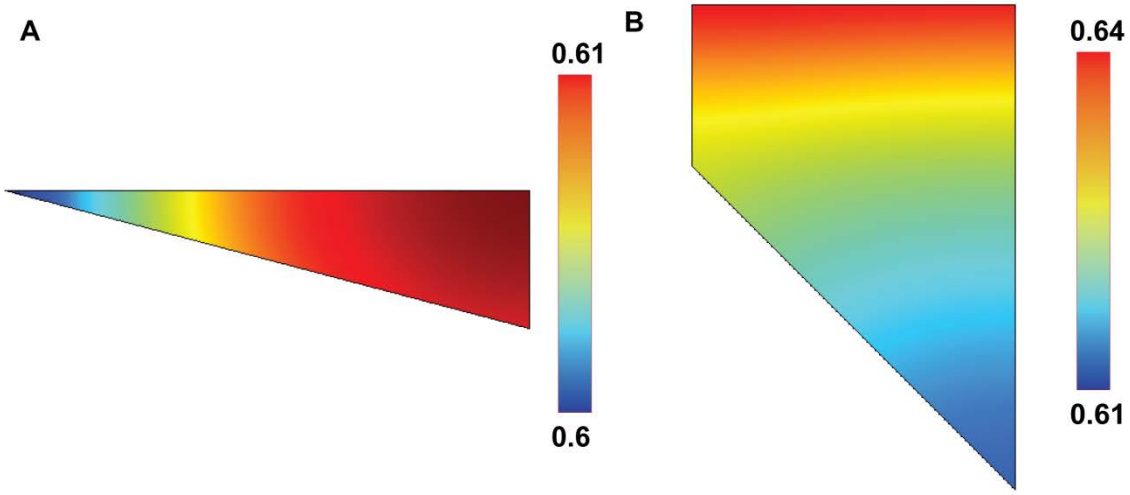

Supplementary Figure 1. 2D gradients of signaling molecule A in A) triangle and B) trapezium. Eq. 1 was solved in COMSOL Multiphysics software using finite-element approaches.

SUPPLEMENTARY FIGURE 2

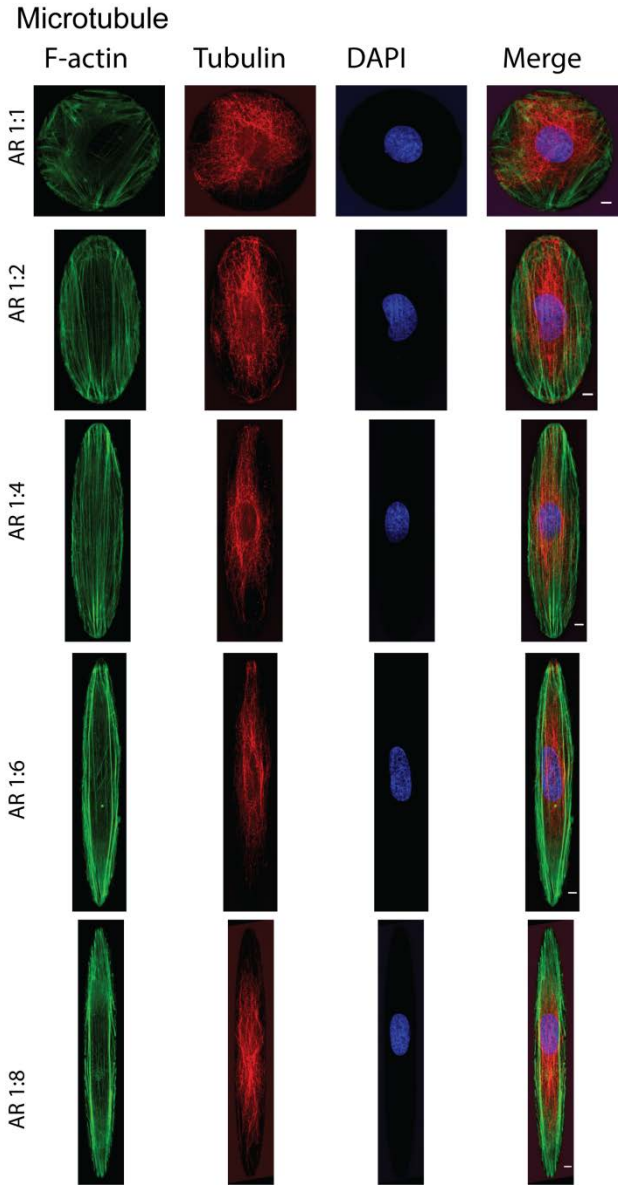

Supplementary Figure 2. Microtubule organization in VSMC with AR 1:1 to A 1:8. Shown are staining of F-actin (green), alpha-tubulin (red) and DAPI in VSMC complying with AR 1:8.

SUPPLEMENTARY FIGURE 3

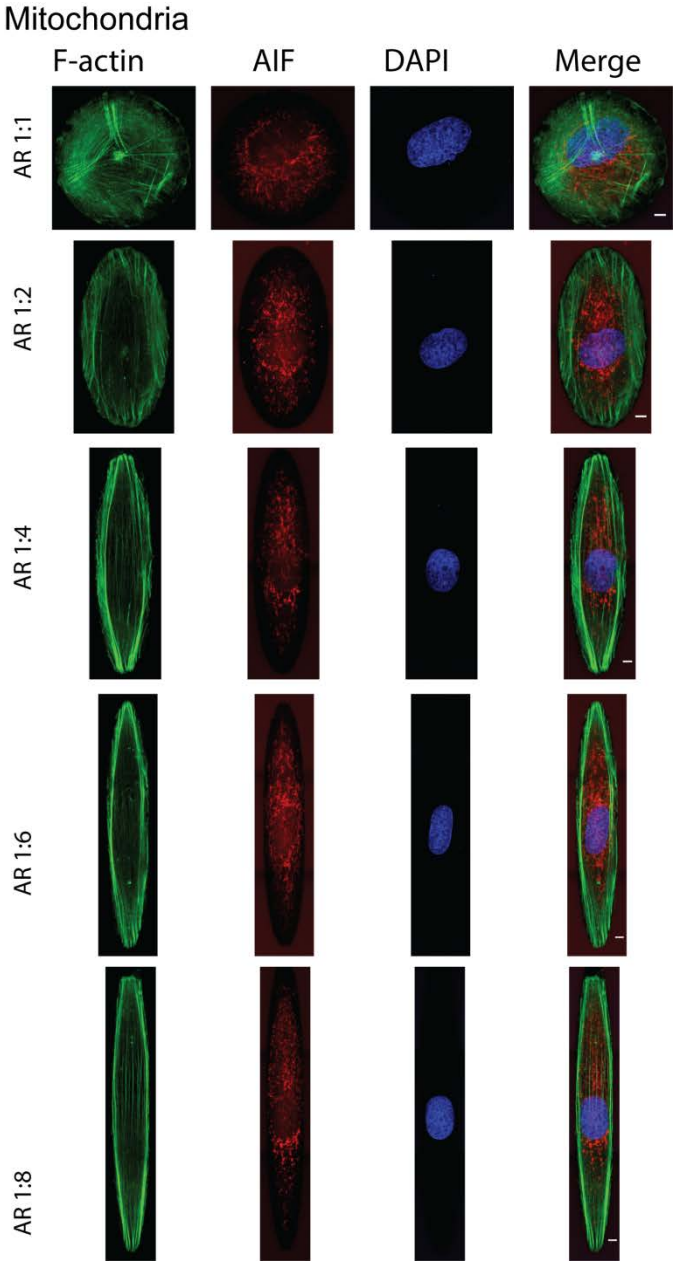

Supplementary Figure 3. Mitochondrial organization in VSMC with AR 1:1 to A 1:8. Shown are staining of F-actin (green), mitochondrial marker Apoptosis Inducing Factor (AIF) (red) and DAPI in VSMC complying with AR 1:8.

SUPPLEMENTARY FIGURE 4

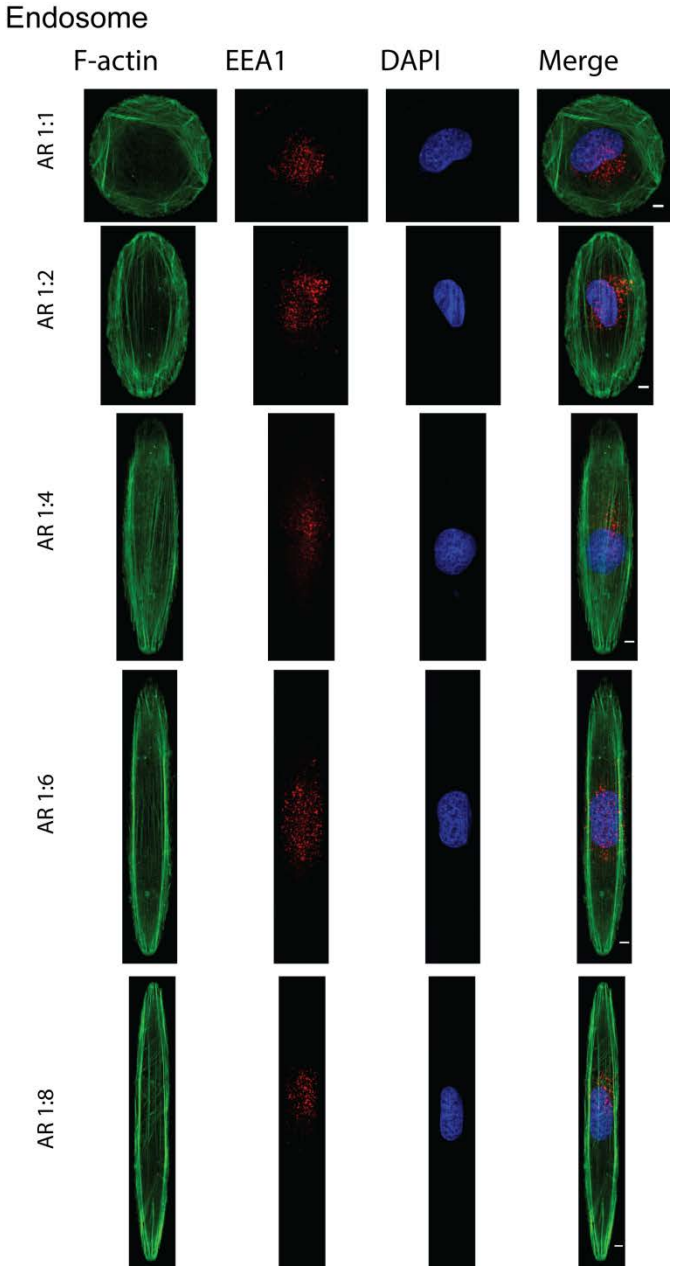

Supplementary Figure 4. Early endosome organization in VSMC with AR 1:1 to A 1:8. Shown are staining of F-actin (green), endosomal marker Early Endosome Antigen 1 (EEA) (red) and DAPI in VSMC complying with AR 1:8.

SUPPLEMENTARY FIGURE 5

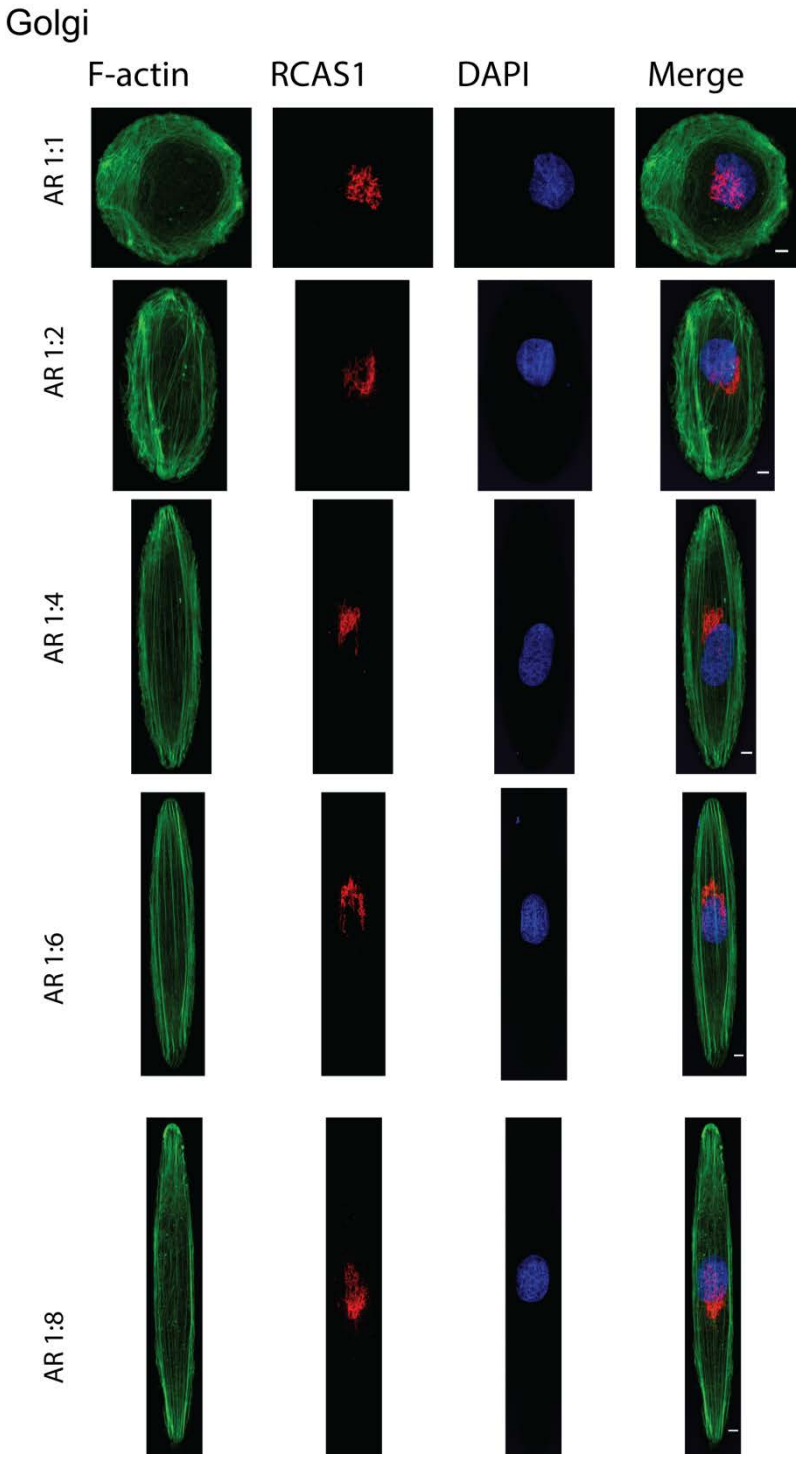

Supplementary Figure 5. Golgi organization in VSMC with AR 1:1 to A 1:8. Shown are staining of F-actin (green), Golgi marker, receptor-binding cancer antigen expressed on SiSo cells (RCAS1) (red) and DAPI in VSMC complying with AR 1:8.

SUPPLEMENTARY FIGURE 6

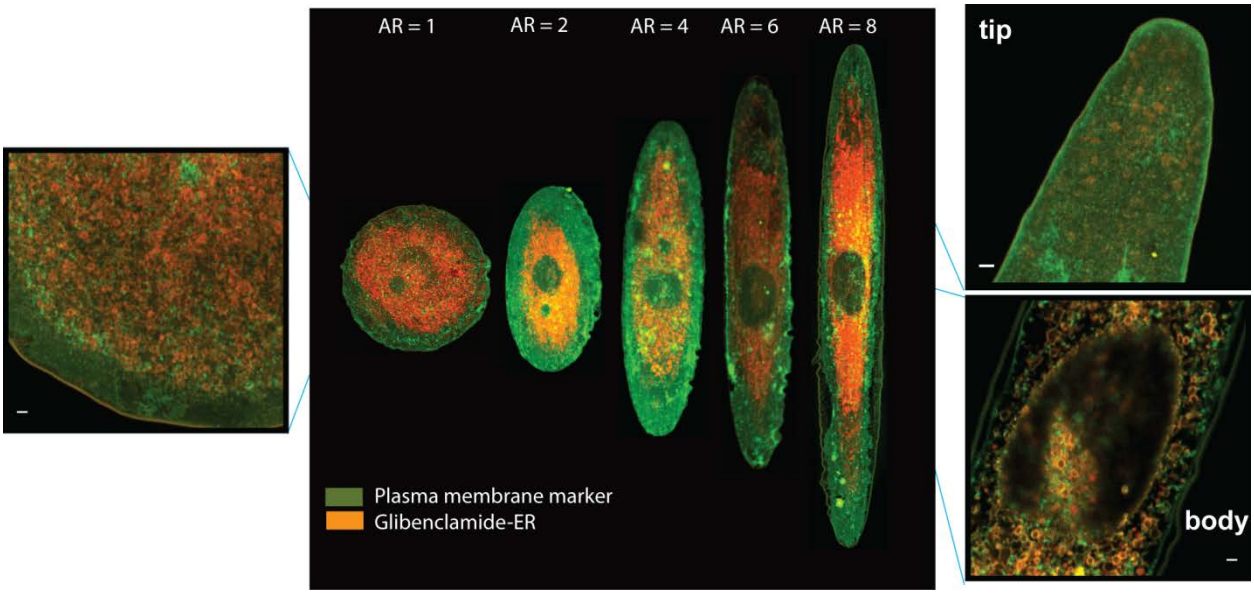

Supplementary Figure 6. Live cell Airy Scan imaging of SR membrane in VSMC with AR 1:1 to A 1:8. Shown are confocal and Airy scan images (inset) of plasma membrane marker (CellMask Plasma Membrane marker, Invitrogen), green and SR marker (Bodipy-Glibenclamide ER) in red.

SUPPLEMENTARY FIGURE 7

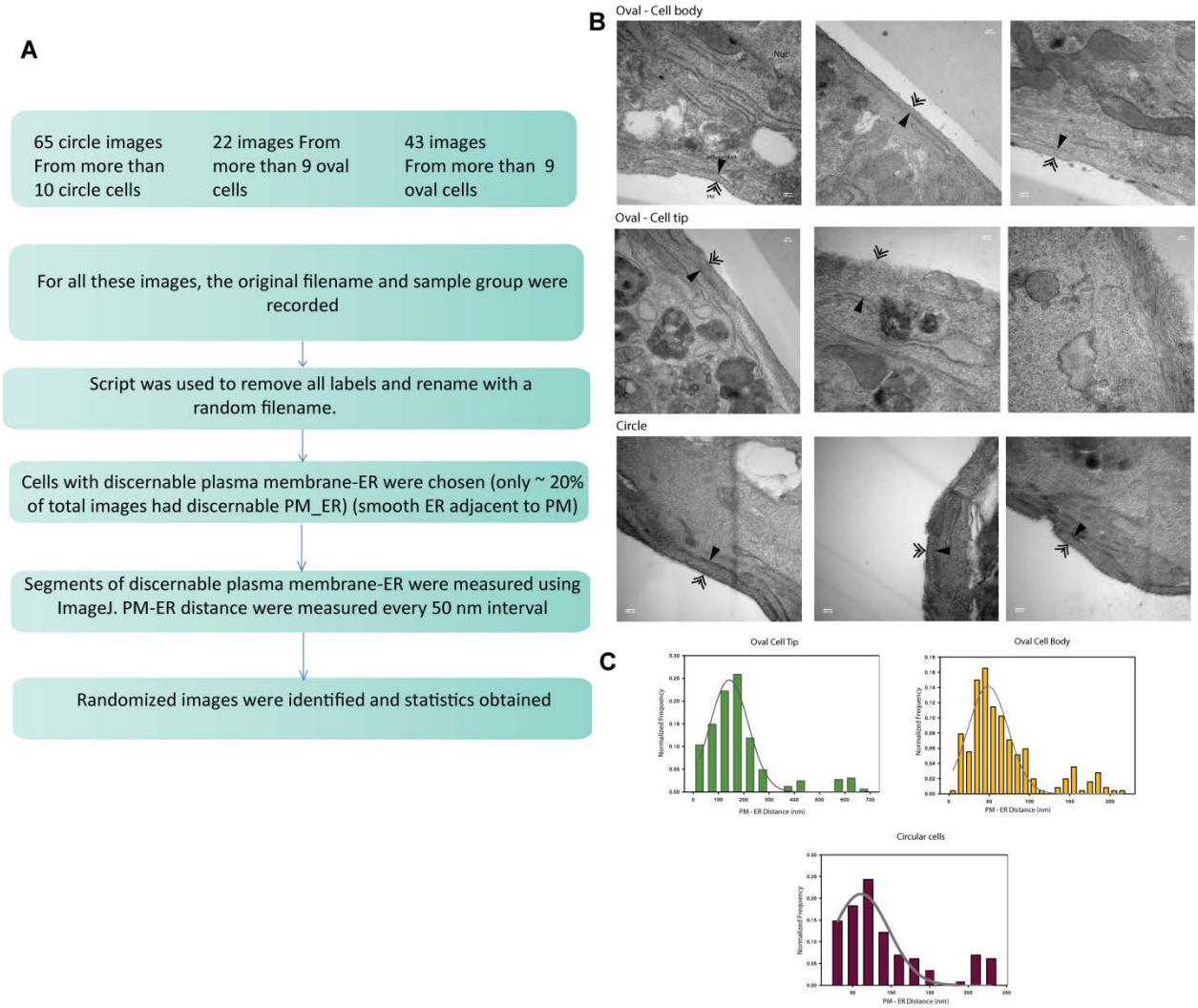

Supplementary Figure 7. TEM quantification of PM-SR distances from electron micrographs. Peripheral SR was identified by its close apposition to the plasma membrane and the absence of attached ribosomes. PM-peripheral SR was measured at 50-nm intervals. A) Post-imaging processing of EM micrographs to quantify PM-SR distances B) Representative images of cells from elliptical cell body, elliptical cell tip and circular cell tip. C) Histograms of distances obtained.

SUPPLEMENTARY FIGURE 8

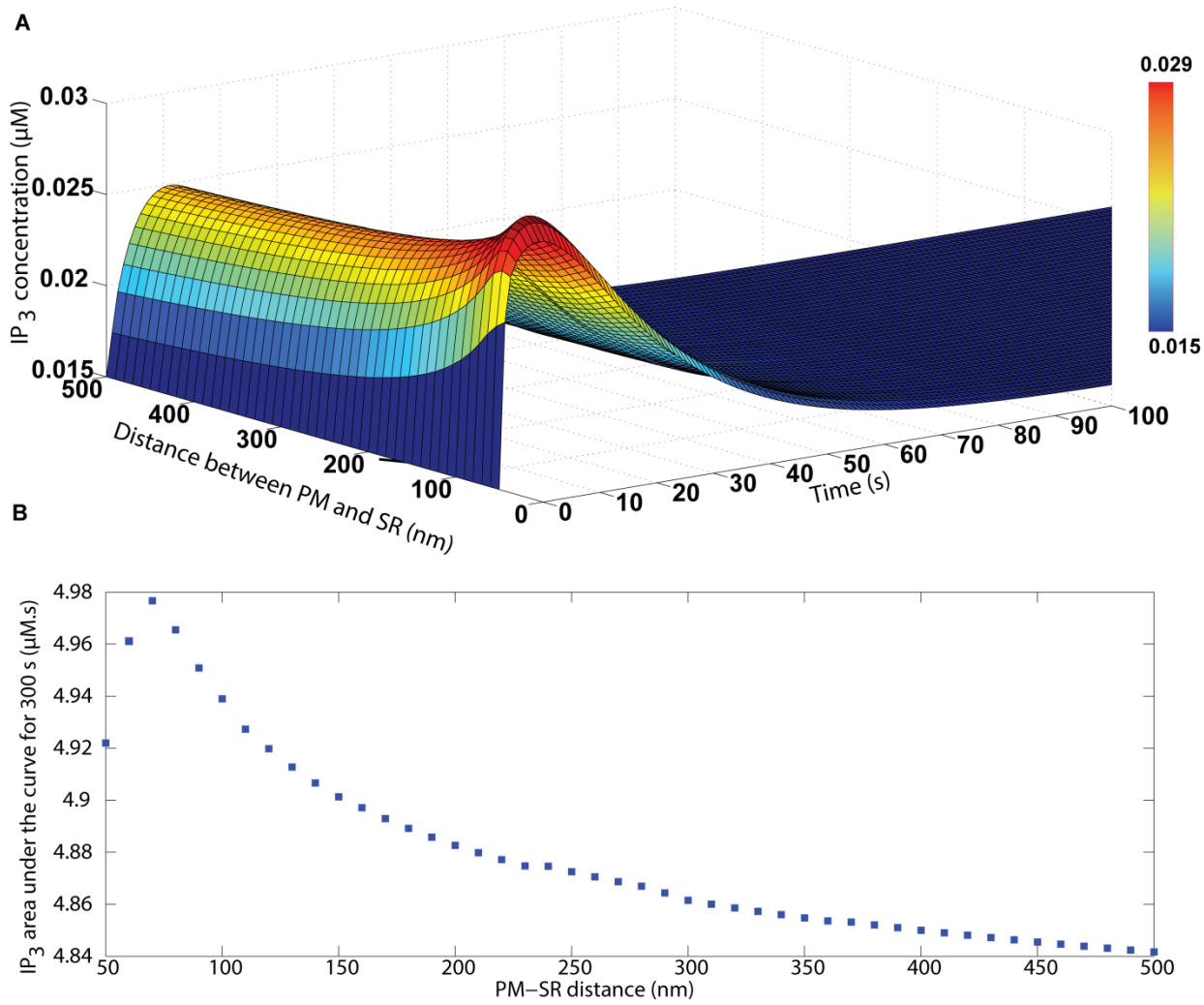

Supplementary Figure 8 The spatio-temporal profile of IP_3 at in different PM-SR distances and resulting AUC. IP_3 concentration, at a location between the PM and SR, as a function of time for different PM-SR distances in rectangular geometries shown in Figure 3B. (B) AUC for IP_3 shows an increase between 50 and 80 nm with a peak at 70 nm and decreases for increasing PM-SR distances from there on, suggesting that the small PM-SR distances are best suited for IP_3 signaling.

SUPPLEMENTARY FIGURE 9

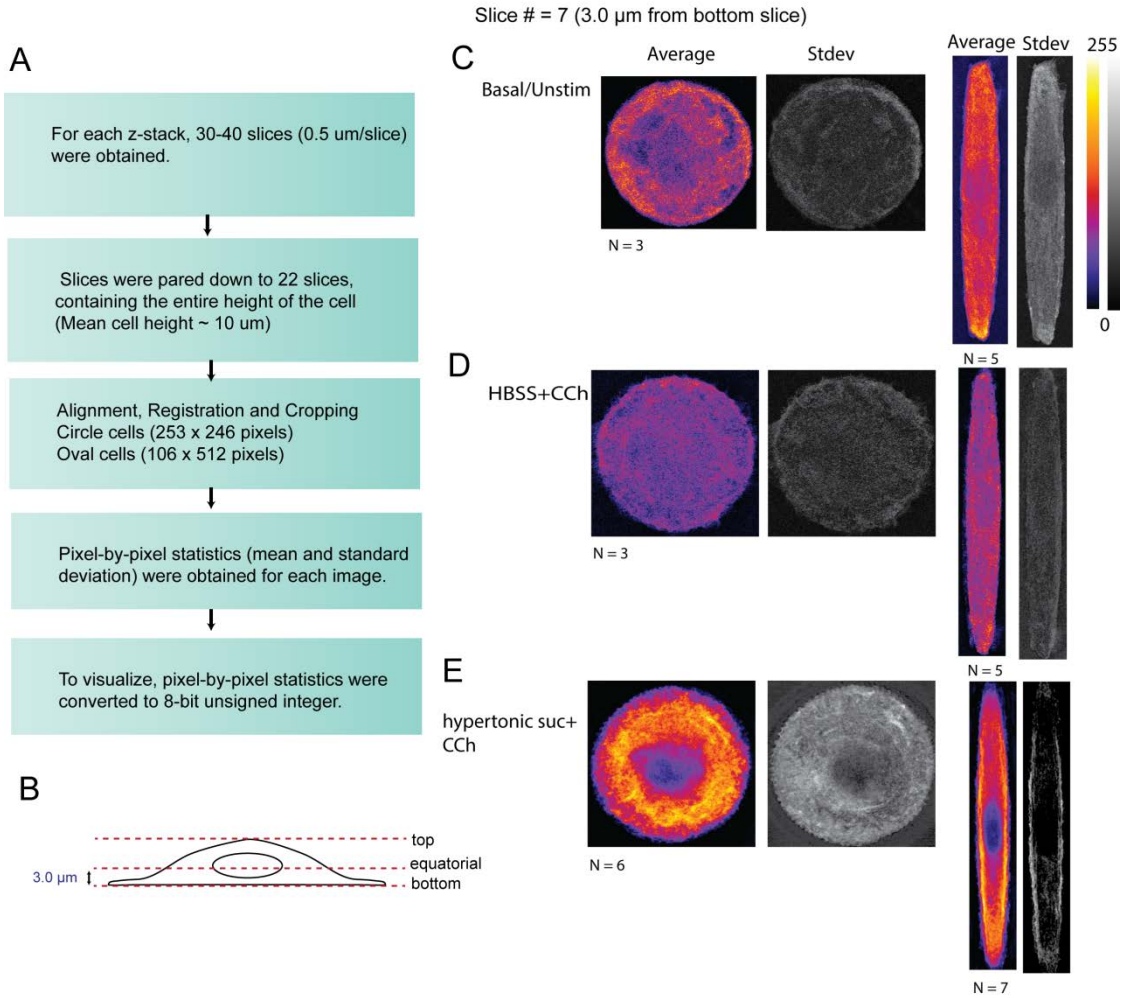

Supplementary Figure 9. Quantitative Immunofluorescence workflow to determine distribution of M3R under different conditions. A) Processing of Z-stacks obtained from individual cells B) Images were obtained at z = 3.0 µm from the bottom of the cell. Representative images obtained at C) basal/unstimulated D) stimulated with 10 µM Carbachol in HBSS and E) Stimulated with 10 µM Carbachol in the presence of hypertonic sucrose at 4 ºC to inhibit receptor endocytosis.

SUPPLEMENTARY FIGURE 10

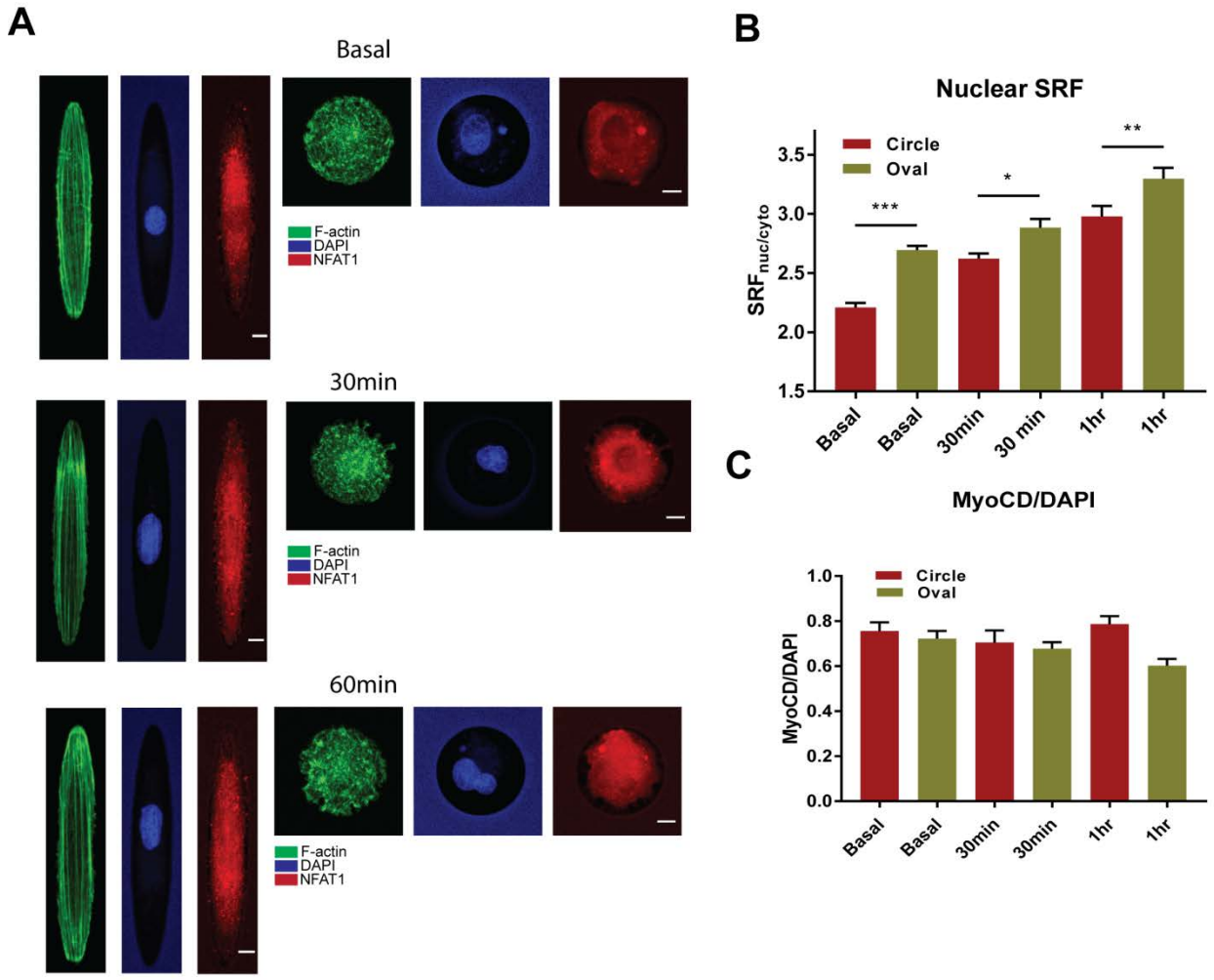

Supplementary Figure 10. NFAT and SRF are impacted by changes in shape while myocardin is not. A) Representative images of NFAT after stimulation with carbachol showing nuclear translocation of NFAT. B) SRF localization into nucleus is impacted by cell shape (shown are mean $\pm$ SEM, $N_{circle,}^{basal}$ = 118, $N_{oval,}^{basal}$ = 120, $N_{circle,}^{30min}$ = 152, $N_{oval,}^{30min}$ = 133, $N_{circle,}^{1hr}$ = 99, $N_{oval,}^{1hr}$ = 132), C) MyoCD was constitutively in the nucleus. No change in myocd nuclear increase was seen with carbachol stimulation (shown are mean $\pm$ SEM, $N_{circle,}^{basal}$ = 17, $N_{oval,}^{basal}$ = 5, $N_{circle,}^{30min}$ = 9, $N_{oval,}^{15min}$ = 17, $N_{circle,}^{1hr}$ = 26, $N_{oval,}^{1hr}$ = 13).

SUPPLEMENTARY FIGURE 11

A

Cell Aspect Ratio	Compartment	Area (μm^2)	Perimeter (μm)
1:1	Cytoplasm	512	158
	ER	1301	446
	Nucleus	153	44
1:2	Cytoplasm	512	172
	ER	1297	310
	Nucleus	153	44
1:4	Cytoplasm	512	215
	ER	1293	390
	Nucleus	155	45
1:6	Cytoplasm	512	255
	ER	1300	460
	Nucleus	155	45
1:8	Cytoplasm	512	290
	ER	1304	511
	Nucleus	152	48
1:10	Cytoplasm	512	320
	ER	1307	582
	Nucleus	154	48

B

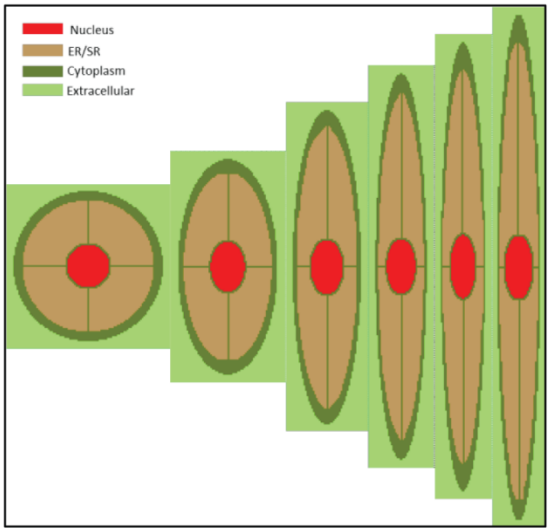

Supplementary Figure 11. A) Geometric region details used for the spatial model using *Virtual Cell* and B) resulting 2D geometries with increasing aspect ratio.

SUPPLEMENTARY FIGURE 12

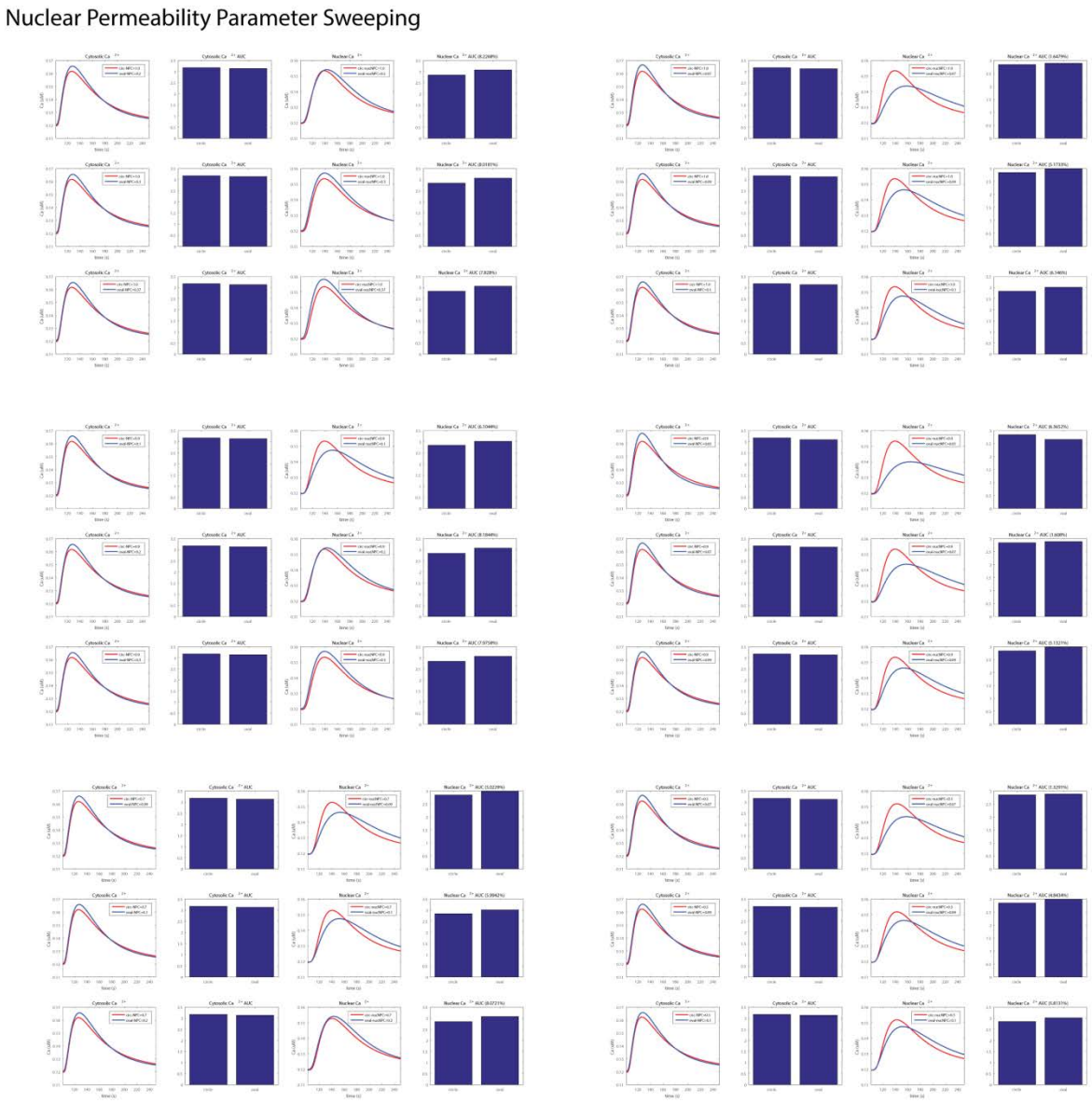

Supplementary Figure 12. Parameter sweep of nuclear permeability in oval and circular geometries. Spatial model was adjusted to include nuclear permeability constant (NPC) to account for nuclear invaginations that could account for variability. NPC was scanned from 0 (completely impermeable) to 1 (completely permeable) in circle and oval geometries and both nuclear and Ca^{2+} dynamics were obtained.

SUPPLEMENTARY INFORMATION

Curvature regulates subcellular organelle location to control intracellular signal propagation

Authors: Rhodora C. Calizo[1], Amit Ron[2], Mufeng Hu[2], Smiti Bhattacharya[2], William G.M. Janssen[1], James Hone[2], Suzanne Scarlata[3], Padmini Rangamani[4]*, Ravi Iyengar [1]*

Affiliations:

[1] Department of Pharmacological Sciences and Systems Biology Center New York, Icahn School of Medicine at Mount Sinai, New York, NY 10029
[2]Department of Mechanical Engineering, Columbia University, New York, NY 10027.
[3]Department of Chemistry and Biochemistry, Worcester Polytechnic Institute, Worcester, MA 01609.
[4]Department of Mechanical and Aerospace Engineering, University of California San Diego, La Jolla, CA 92093.

*To whom correspondence should be addressed:

Ravi Iyengar, Ph.D.
Department of Pharmacological Sciences
Icahn School of Medicine at Mount Sinai
One Gustave L. Levy Place, Box 1215
New York NY 10029
Phone: 212-659-1707
Fax: 212-831-0114
e-mail: ravi.iyengar@mssm.edu

or

Padmini Rangamani, Ph.D.
Department of Mechanical and Aerospace Engineering
University of California San Diego
La Jolla, CA 92093
Phone: 858-534-4734
e-mail: prangamani@ucsd.edu

NUMERICAL SOLUTIONS FOR REACTION DIFFUSION EQUATIONS WITH ROBIN BOUNDARY CONDITIONS.

We investigate the dynamics of a molecule A, which is formed at the PM and freely diffuses in the cytoplasm and is consumed at the SR membrane. This phenomenon can be represented by the following reaction-diffusion equation with the accompanying boundary conditions.

$$\frac{\partial[A]}{\partial t} = D_A \nabla^2[A] - k_{deg}[A]$$

$$D(\mathbf{n} \cdot \nabla[A])|_{PM} = k_{on}[A]|_{PM}$$

$$D(\mathbf{n} \cdot \nabla[A])|_{SR} = -k_{off}[A]|_{SR}$$

One of the features of this system of equations is that the boundary conditions at both ends are time-dependent and belong to a class of boundary conditions known as Robin boundary conditions[29]. Furthermore, the boundary conditions depend on the local shape, since the surface normal will change as a function of curvature[72]. If the boundary conditions at both membranes were constant values of the concentration of A, the solution to the partial differential equation (Eq. 1) is a linear distribution from one boundary to the other[29]. However, in the current case, where both boundary conditions have Robin boundary conditions, the solution to these equations depends *both* on the diffusion distance and the reaction rates. The Robin boundary conditions that accompany the reaction-diffusion equation are of the mixed-type and are time dependent. Therefore, writing analytical solutions for them is challenging. Therefore, we use numerical methods to solve this equation. We use finite-element methods to solve the equations in the commercially available software COMSOL Multiphysics®.

Briefly, we used the General Form PDE interface to model the partial differential equation and the flux boundary conditions implemented using the Flux node with the source term set to the reaction rate. We used three different geometries to test the role of curvature and PM-SR distance. The mesh size was set to 'Extremely Fine' and the tolerance was set to relative tolerance was set to 0.01. In addition to the geometries shown in Fig. 1A, simulations were also conducted for a triangle and a trapezium to analyze the effect of varying PM-SR distance without changing curvature (Supplementary Fig. 1).

For a rectangle and a circle, solving the PDE with the boundary conditions shown above amounts to solving a 1-dimensional problem (either in the z-direction or in the radial direction). As a result, a gradient is observed only in one direction. For an elliptical cross section (Fig. 1A), a triangle (Supplementary Fig. 1A) and a trapezium (Supplementary Fig. 1B), the geometric variation is in two-dimensions. Therefore, the spatio-temporal dynamics of A is different in these patterns. Furthermore, in an ellipse, the curvature is varying along the membrane, and therefore, the diffusive flux also varies. This is because the diffusive flux is dependent on the local normal and curvature captures the rate of change of the normal along the curve[72].

Dimensional analysis

Using the PM-SR distance 'L' as a characteristic length scale and k_{deg} as the characteristic time scale, we non-dimensionalized the partial differential equation for A to obtain a dimensionless number $D/(k_{deg}L^2)$ which is the Damkohler number[29]. When the Damkohler number is much greater than 1, then the system is diffusion-dominated and when the Damkohler number is much less than 1, it is reaction-dominated.

IP_3 model implementation in COMSOL

The dynamics of IP_3 were modeled using the reaction network model presented in Cooling et al.[73] and implemented in COMSOL using the protocol presented in Vollmer et al.[74]. We modeled multiple

compartments – the extracellular space, PM, SR, SR membrane, the nucleus and the nuclear membrane. The Robin boundary conditions were implemented using the Flux boundary condition node for the volume and the general boundary form PDE node for the membranes. The mesh size was set to 'Extremely fine' such that the minimum element size is 0.1 nm and relative tolerance was set to 0.01. These values of mesh size and tolerance were chosen such that smaller values of tolerance or mesh refinement didn't alter the numerical results.

INTEGRATIVE WHOLE-CELL REACTION-DIFFUSION MODEL

To understand how global cell shape can modulate the dynamics of IP_3 and calcium signaling, we developed mathematical models which analyze the relationships between the binding of extracellular ligand to GPCR, G-protein activation and cycling, PLCβ activation, IP_3 activation of IP_3R in the SR and intracellular calcium dynamics. Reactions were initially implemented as a system of ordinary differential equation in the Virtual Cell environment (http://www.nrcam.uchc.edu/)[75], and then modeled as a system of partial differential equations (PDEs) in two-dimensions. The complete list of model equations, parameters, units and references of the kinetic parameters are listed in Table 1 and the complete list of initial conditions and diffusion coefficients are listed in Table 2.

GPCR Signaling-PLCβ cycling

We adapted the GPCR signaling modules described by Cooling et al.[73] with modifications. Reactions R1-R6 represent GPCR-Ligand-G protein interactions on the plasma membrane. The reactions are modeled as kinetic fluxes following the Law of Mass Action and Michaelis-Menten Kinetics (see Bhalla[2]). The binding of extracellular ligand to cell-surface receptors are represented by reactions R1 and R4. Binding of the ligand to muscarinic acetylcholine receptors causes a conformational change on the $G\alpha_q$ subunit of the heterotrimeric G-protein, causing replacement of GDP with GTP (R7) and dissociation of the Gα subunit from the heterotrimeric G-protein. The binding of activated $G\alpha_q$ to the enzyme PLCβ are represented by R8 and R10. $G\alpha_q$-GTP is hydrolyzed to $G\alpha_q$-GDP by autocatalysis represented by R7. Reactions R13-R16 represent IP3 dynamics, including its production at the plasma membrane, membrane diffusion and degradation at the cytosol. R13 and R14 shows the hydrolysis of PIP2 to IP3 by PLCβ-Ca^{2+} and PLCβ-Ca^{2+}-$G\alpha_q$(GTP) respectively. The degradation of IP3, which involves the dephosphorylation and phosphorylation of IP3 to form inositol biphosphate and inositol tetraphosphate are represented by R16. The metabolic recycling of IP3 from these products is not considered. PLCβ inactivation is represented by R5.

IP_3/Calcium Dynamics

In vascular smooth muscle cells, agonist-induced calcium release from the SR/ER is the main source of intracellular Ca^{2+} transient. The opening of the inositol triphosphate receptor channels (IP_3R) from the ER membrane, leads to an increase in cytoplasmic calcium. We used the simplified version of channel kinetics [76, 77] by De Young and Keizer [78] which is represented by R17. Calcium leak from the ER to the cytosol is represented by R18. Calcium is pumped back to the ER by the sarcoplasmic reticulum calcium ATPase (SERCA) pump, represented by R19. Calcium leaks to the extracellular space through an Na^+/Ca^{2+} exchanger (NCX), (R22), and plasma membrane calcium ATPase (PMCA) pump R23. IP3 dependent influx of calcium through the plasma membrane is represented by $J_{PM,leak}$ which is dependent on IP3. Rapid buffering kinetics of Calcium [79] by exogenous and endogenous calcium buffers, is assumed.

Geometries

The spatial geometries of the cell and organelles were depicted as idealized geometries represented as a series of concentric ellipsoids that represent whole cell, SR and the nucleus. We assumed that cells complying with shapes of increasing AR conserve the cell volume and increase the plasma membrane surface area with increasing AR. Hence, whole cell, cytoplasmic and SR areas were kept constant with

increasing aspect ratios. The cellular geometries were approximated from experimentally observed VSMC confined from AR 1:1 to AR 1:8 (Figure 2), whereby the SR is closer to the PM in the perinuclear region compared to the cell tips. Furthermore, as the aspect ratio increased, both PM-SR and PM-nuclear distances decreased in the minor axis and increased in the major axis of the ellipse. Nuclear shapes were based on experimentally observed geometries (Fig. 2h-n). Figure S11 show the geometric details of each compartment (Supplementary Fig. 11A) and the resulting geometries (Supplementary Fig. 11B). To solve the PDEs, geometries were discretized into 0.5 µm x 0.5 µm spatial steps, resulting in a total area of 3,500 μm^2 (10,500 elements). The systems of equations were solved within the Virtual Cell framework using fully-implicit, finite volume, with variable time step solver, with a maximum time step of 0.1 s and an output interval of 1.0 second.

Supplementary Table 1. Model reactions and parameter values

Reaction	Description	Model equation	Parameter	Value	Units	Reference
		Membrane Receptor Reactions				
R1	Ligand + GPCR <-> Ligand-GPCR *Ligand binding*	Kf_{r1}[Ligand] [GPCR_cyto_mem] - Kr_{r1}[L_GPCR_cyto_mem]	Kf_{r1} Kr_{r1}	3.00 x 10^{-4} 4.50 x 10^{-7}	μM s^{-1}	Cooling [73] Lukas [80]
R2	Ligand-GPCR + G-protein <-> Ligand-GPCR-G-protein *GPCR cycling*	Kf_{r2}[G_protein][L_GPCR_cyto_mem] - Kr_{r2}[Ligand_GPCR_G_cyto_mem]	Kf_{r2} Kr_{r2}	3.00 x 10^{-1} 9.00 x 10^{-6}	μM s^{-1}	Cooling [73] Lukas [80]
R3	GPCR + G-protein <-> GPCR-G-protein *GPCR cycling*	Kf_{r3}*[G_protein][GPCR_cyto_mem] -* Kr_{r3}*[GPCR_G_cyto_mem]*	Kf_{r3} Kr_{r3}	2.75 x 10^{-4} 7.54 x 10^{0}	μM s^{-1}	Cooling [73] Lukas [80]
R4	GPCR-G-protein + Ligand <-> Ligand-GPCR-G-protein *Ligand binding*	Kf_{r4}*[GPCR_G_cyto_mem_ligand] -* Kr_{r4}*[L_GPCR_G_cyto_mem]*	Kf_{r4} Kr_{r4}	6.02 x 10^{-1} 9.02 x 10^{-4}	μM s^{-1}	Cooling [73] Lukas [80]
R5	Ligand-GPCR-G-protein <-> Ligand-GPCR-Gαq* *Gαq activation*	Kf_{r5}*[L_GPCR_G_cyto_mem] -* Kr_{r5}*[G_a_q_mem][L_GPCR_cyto_mem]*	Kf_{r5} Kr_{r5}	2.22 x 10^{1} 0.00 x 10^{0}	μM s^{-1}	Cooling [73] Lukas (2)
R6	Ligand-GPCR-G-protein <-> Ligand- GPCR-p-G-protein *GPCR phosphorylation*	Kf_{r6}*[L_GPCR_G_cyto_mem] -* Kr_{r6}*[ligand_GPCR_p_cyto_mem]*	Kf_{r6} Kr_{r6}	6.22 x 10^{-2} 0.00 x 10^{0}	μM s^{-1}	Cooling [73] Lukas (2)
R7	Gαq* <-> Gαq-GDP *Gαq deactivation*	Kf_{r7}*[G_a_q_mem] -* Kr_{r7}*[G_GDP_mem]*	Kf_{r7} Kr_{r7}	1.50 x 10^{-1} 0.00 x 10^{0}	μM s^{-1}	Cooling (1) Lukas (2)
R8	Gαq* + PLCβ <-> PLCβ-Gαq *Gαq binding to PLCβ*	Kf_{r8}*[PLC_inactive][G_a_q_mem] -* Kr_{r8}*[PLC_Ga]*	Kf_{r8} Kr_{r8}	4.20 x 10^{-2} 1.00 x 10^{0}	μM s^{-1}	Cooling (1) Lukas (2)
R9	Ca + PLCβ <-> PLCβ-Ca *Calcium binding to PLCβ*	Kf_{r9}*[PLC_inactive]*[$Calcium_{cyto}$] - Kr_{r9}*[PLC_Ca]*	Kf_{r9} Kr_{r9}	1.67 x 10^{-2} 1.67 x 10^{-2}	μM s^{-1}	Cooling [73] Lukas (2)
R10	Gαq*+PLCβ-Ca <-> PLC-Gq_Ca *PLCβ activation by Gαq*	Kf_{r10}*[PLC_Ca][G_a_q_mem] -* Kr_{r10}*[PLC_Ca_Ga]*	Kf_{r10} Kr_{r10}	4.20 x 10^{-2} 1.00 x 10^{0}	μM s^{-1}	Cooling [73] Lukas (2)
R11	Ca + PLCβ-Gq <-> PLCb-Gq-Ca *PLCβ activation by Gαq*	Kf_{r11}*[PLC_Ga]*[$Calcium_{cyto}$] - Kr_{r11}*[PLC_Ca_Ga]*	Kf_{r11} Kr_{r11}	3.34 x 10^{-5} 3.34 x 10^{-5}	μM s^{-1}	Cooling [73] Lukas (2)
R12	PLCβ-Gq <-> Gαq-GDP + PLCβ *PLCβ dissociation from Gαq*	Kf_{r12}*[PLC_Ca_Ga] -* Kr_{r12}*[PLC_Ca * G_GDP_mem]*	Kf_{r12} Kr_{r12}	6.00 x 10^{0} 0.00 x 10^{0}	μM s^{-1}	Cooling [73] Lukas (2)
		PIP_2/IP_3 Metabolism				
R13	PIP_2 + PLCβ-Gq-Ca <-> IP_3 + DAG *PIP_2 hydrolysis by PLCβ*	$\frac{Kcat_{r13}[PLC\beta_Gq_Ca][PIP_2]}{Km_{r13} + [PIP_2]}$	$Kcat_{r13}$ Km_{r13}	1.20 x 10^{1} 1.98 x 10^{1}	s^{-1} μM	Cooling [73] Bhalla [2]
R14	PIP_2 + PLCβ-Ca <-> IP_3 + DAG *PIP_2 hydrolysis by PLCβ*	$\frac{Kcat_{r14}[PLC\beta_Ca][PIP_2]}{Km_{r14} + [PIP_2]}$	$Kcat_{r14}$ Km_{r14}	3.80 x 10^{0} 5.00 x 10^{0}	s^{-1} μM	Cooling [73] Bhalla (3)
R15	PLCβ* <-> PLCβ *PLCβ inactivation*	Kf_{r15}*[PLCβ_Ca]*	Kf_{r15}	6.00 x 10^{0}	s^{-1}	Cooling [73]

R16	IP_3 <-> IP_3* *IP_3 degradation*	$Kf_{r16}[IP_3]$	Kf_{r16}	3.00×10^{-2}	s^{-1}	Cooling [73] Lukas (2)
		Calcium Signaling				
β_i	Calcium buffering (fast reaction assumption)	$\left(1.0 + \frac{Pr_{tot_e} Km_e}{Km_e \left[Calcium_{cyto}\right]^2} + \frac{Pr_{tot_x} Km_x}{Km_x \left[Calcium_{cyto}\right]^2}\right)^{-1}$	Pr_{tot_e} Km_e Pr_{tot_x} Km_x	1.91×10^{2} 2.43×10^{0} 8.77×10^{0} 1.39×10^{-1}	µM µM µM µM	Wagner [79] Maurya [81] Experiment
R17	IP3 + IP3R <-> $Calcium_{cyto}$ + IP3 + IP3R *IP3R channel open probability*	$-\beta_i \left(\frac{[IP3]\,[Calcium_{cyto}]\,h}{([IP_3] + Ki_{r17})([Calcium_{cyto}] + Kact_{r17})}\right)^3$ $\left(1 - \frac{[Calcium_{cyto}]}{[Calcium_{ER}]}\right)(Jmax_{r17})$	Ki_{r17} $Kact_{r17}$ $Jmax_{r17}$	8.00×10^{-1} 2.00×10^{-1} 3.50×10^{-3}	µM µM µM s^{-1}	De-Young & Keizer [78] Maurya (5) Fink [77] Li [76]
		$h = ((K1_{r17} - (([Calcium_{cyto}] + K1_{r17})h))K2_{r17}$	$K1_{r17}$ $K2_{r17}$	1.10×10^{-1} 2.10×10^{0}	- -	
R18	Ca_ER <-> Ca_cyt *Calcium leak from ER to cytosol*	$-\beta_i \left(1.0 - \frac{[Calcium_{cyto}]}{[Calcium_{ER}]}\right) L_{r18}$	L_{r18}	5.60×10^{-2}	µM s^{-1}	Fink (7) Keener [82]
R19	Ca_cyt <-> Ca_ER *SERCA pump activity*	$\beta_i \frac{Vmax_{r19}\,[Calcium_{cyto}]^2}{[Calcium_{cyto}]^2 + Kp_{r19}^2}$	$Vmax_{r19}$ Kp_{r19}	1.59×10^{0} 2.70×10^{-1}	µM s^{-1} µM	Fink (7) Keener (9)
R20	Ca_ECM -> Ca_cyt *IP3 dependent calcium channels*	$\beta_i \frac{Vmax_{r20}\,[IP_3]^2}{Km_{r21}{}^2 + [IP_3]^2}$	$Vmax_{r20}$ Km_{r20}	1.00×10^{0} 1.00×10^{0}	µM s^{-1} µM	Maurya (5)
R21	Ca_cyt <-> Ca_extracellular *Calcium leak through the plasma membrane*	$\beta_i\, Vpm_{r21}$	Vpm_{r21}	1.00×10^{-2}	s^{-1}	Maurya (5)
R22	Ca_cyt -> Ca_ECM *Sodium calcium channel (NCX) activity*	$\beta_i \frac{Vmax_{r22}\,[Calcium_{cyto}]}{[Calcium_{cyto}] + Km_{r22}}$	$Vmax_{r22}$ Km_{r22}	1.00×10^{-1} 1.00×10^{-1}	µM s^{-1} µM	Maurya (5)
R23	Ca_cyt -> Ca_ECM *PMCA pump activity*	$\beta i \left(\frac{Vmax_{l_{r23}}[Calcium_{cyto}]^2}{[Calcium_{cyto}]^2 + Km_{l_{r23}}{}^2} + \frac{Vmax_{h_{r23}}[Calcium_{cyto}]^5}{[Calcium_{cyto}]^5 + Km_{h_{r23}}{}^5}\right)$	$Vmax_{l_r23}$ Km_{l_r23} $Vmax_{h_r23}$ Km_{h_r23}	1.13×10^{-1} 4.42×10^{-1} 5.90×10^{-1} 4.42×10^{-1}	µM s^{-1} µM µM s^{-1} µM	Maurya (5) Weisner [83]

Supplementary Table 2. Initial Concentration and Diffusion coefficient of reactants.

Species	Initial Concentration (μM)	Diffusion Coefficient ($\mu m^2/s$)	References
Calcium	0.1 μM	220	Knot, Cooling[73, 84]
IP3	0.015 μM	10	Cooling, Dickinson[61, 73]
Ligand	10 μM	-	Agonist added
Calcium_nuc	0.122 μM	220	Value obtained after equilibriation
Calcium_ER	400 μM	220	Fink[77, 85]
Receptor	2.93 μm^{-2}	0.1	Cooling, Bers[73, 86]
L_R_GD	0 μm^{-2}	0.1	Unstimulated state
R_GD	1.07 μm^{-2}	0.1	Cooling, Bers[73, 86]
GT	0 μm^{-2}	0.1	Unstimulated state
GD	10000 μm^{-2}	0.1	Cooling, Lukas[73, 80]
PLC	90.9 μm^{-2}	0.1	Cooling, Lukas[73, 80]
PLC_GT	0 μm^{-2}	0.1	Unstimulated state
PIP2	4000 μm^{-2}	2.5	Cooling, Xu, Golebiewska[73, 87, 88]
LR	0 μm^{-2}	0.1	Unstimulated state
PLC_Ca	9.09 μm^{-2}	0.1	Cooling, Lukas[73, 80]
PLC_Ca_GT	0 μm^{-2}	0.1	Unstimulated state
L_R_GD_P	0 μm^{-2}	0.1	Unstimulated state
Rinh	7.7825 μm^{-2}	0.1	Fink, Eungdamrong[77, 85, 89]
Ract	9.056 μm^{-2}	0.1	Fink, Eungdamrong[77, 85, 89]
RinhCa	3.5375 μm^{-2}	0.1	Fink, Eungdamrong[77, 85, 89]
RactCa	2.264 μm^{-2}	0.1	Fink, Eungdamrong[77, 85, 89]
SERCA	45 μm^{-2}	0.1	Fink, Eungdamrong[77, 85, 89]
ER_erMembrane	2 μm^{-2}	--	Fink, Eungdamrong[77, 85, 89]

REFERENCES

1. Neves, S.R., Ram, P.T. & Iyengar, R. G protein pathways. *Science* **296**, 1636-1639 (2002).

2. Bhalla, U.S. & Iyengar, R. Emergent properties of networks of biological signaling pathways. *Science* **283**, 381-387 (1999).

3. Rangamani, P. *et al.* Decoding information in cell shape. *Cell* **154**, 1356-1369 (2013).

4. Neves, S.R. *et al.* Cell shape and negative links in regulatory motifs together control spatial information flow in signaling networks. *Cell* **133**, 666-680 (2008).

5. Meyers, J., Craig, J. & Odde, D.J. Potential for control of signaling pathways via cell size and shape. *Current biology* **16**, 1685-1693 (2006).

6. Kholodenko, B.N. Spatially distributed cell signalling. *FEBS letters* **583**, 4006-4012 (2009).

7. Vilardaga, J.-P., Jean-Alphonse, F.G. & Gardella, T.J. Endosomal generation of cAMP in GPCR signaling. *Nature chemical biology* **10**, 700-706 (2014).

8. Villaseñor, R., Nonaka, H., Del Conte-Zerial, P., Kalaidzidis, Y. & Zerial, M. Regulation of EGFR signal transduction by analogue-to-digital conversion in endosomes. *Elife* **4**, e06156 (2015).

9. Whitaker, M. Calcium at fertilization and in early development. *Physiological reviews* **86**, 25-88 (2006).

10. Pinton, P., Giorgi, C., Siviero, R., Zecchini, E. & Rizzuto, R. Calcium and apoptosis: ER-mitochondria Ca2+ transfer in the control of apoptosis. *Oncogene* **27**, 6407-6418 (2008).

11. Berridge, M.J. Calcium signalling and cell proliferation. *Bioessays* **17**, 491-500 (1995).

12. Wei, C. *et al.* Calcium flickers steer cell migration. *Nature* **457**, 901-905 (2009).

13. Berridge, M.J. & Taylor, C. in Cold Spring Harbor symposia on quantitative biology, Vol. 53 927-933 (Cold Spring Harbor Laboratory Press, 1988).

14. Hirose, K., Kadowaki, S., Tanabe, M., Takeshima, H. & Iino, M. Spatiotemporal dynamics of inositol 1, 4, 5-trisphosphate that underlies complex Ca2+ mobilization patterns. *Science* **284**, 1527-1530 (1999).

15. Berridge, M.J. Inositol trisphosphate and calcium signalling mechanisms. *Biochimica et Biophysica Acta (BBA)-Molecular Cell Research* **1793**, 933-940 (2009).

16. Brozovich, F.V. *et al.* Mechanisms of vascular smooth muscle contraction and the basis for pharmacologic treatment of smooth muscle disorders. *Pharmacological reviews* **68**, 476-532 (2016).

17. Kudryavtseva, O., Aalkjær, C. & Matchkov, V.V. Vascular smooth muscle cell phenotype is defined by Ca2+-dependent transcription factors. *FEBS journal* **280**, 5488-5499 (2013).

18. Hogan, P.G., Chen, L., Nardone, J. & Rao, A. Transcriptional regulation by calcium, calcineurin, and NFAT. *Genes & development* **17**, 2205-2232 (2003).

19. Miranti, C.K., Ginty, D.D., Huang, G., Chatila, T. & Greenberg, M.E. Calcium activates serum response factor-dependent transcription by a Ras-and Elk-1-independent mechanism that involves a Ca2+/calmodulin-dependent kinase. *Molecular and cellular biology* **15**, 3672-3684 (1995).

20. Wang, D.-Z. *et al.* Activation of cardiac gene expression by myocardin, a transcriptional cofactor for serum response factor. *Cell* **105**, 851-862 (2001).

21. Rensen, S., Doevendans, P. & Van Eys, G. Regulation and characteristics of vascular smooth muscle cell phenotypic diversity. *Netherlands Heart Journal* **15**, 100-108 (2007).

22. Rzucidlo, E.M., Martin, K.A. & Powell, R.J. Regulation of vascular smooth muscle cell differentiation. *Journal of vascular surgery* **45**, A25-A32 (2007).

23. Gomez, D. & Owens, G.K. Smooth muscle cell phenotypic switching in atherosclerosis. *Cardiovascular research*, cvs115 (2012).

24. Chamley-Campbell, J., Campbell, G.R. & Ross, R. The smooth muscle cell in culture. *Physiol rev* **59**, 1-61 (1979).

25. Owens, G.K., Kumar, M.S. & Wamhoff, B.R. Molecular regulation of vascular smooth muscle cell differentiation in development and disease. *Physiological reviews* **84**, 767-801 (2004).

26. Eglen, R.M., Reddy, H., Watson, N. & Challiss, R.J. Muscarinic acetylcholine receptor subtypes in smooth muscle. *Trends in pharmacological sciences* **15**, 114-119 (1994).

27. Caulfield, M.P. Muscarinic receptors—characterization, coupling and function. *Pharmacology & therapeutics* **58**, 319-379 (1993).

28. Berridge, M.J. & Irvine, R.F. Inositol phosphates and cell signalling. *Nature* **341**, 197-205 (1989).

29. Bird, R.B., Stewart, W.E. & Lightfoot, E.N. *Transport phenomena*. (John Wiley & Sons, 2007).

30. Pollard, T.D. & Cooper, J.A. Actin, a central player in cell shape and movement. *Science* **326**, 1208-1212 (2009).

31. McBeath, R., Pirone, D.M., Nelson, C.M., Bhadriraju, K. & Chen, C.S. Cell shape, cytoskeletal tension, and RhoA regulate stem cell lineage commitment. *Developmental cell* **6**, 483-495 (2004).

32. Vogel, V. & Sheetz, M. Local force and geometry sensing regulate cell functions. *Nature reviews Molecular cell biology* **7**, 265-275 (2006).

33. Storm, C., Pastore, J.J., MacKintosh, F.C., Lubensky, T.C. & Janmey, P.A. Nonlinear elasticity in biological gels. *Nature* **435**, 191-194 (2005).

34. Valm, A.M. *et al.* Applying systems-level spectral imaging and analysis to reveal the organelle interactome. *Nature* (2017).

35. Waterman-Storer, C.M. & Salmon, E.D. Endoplasmic reticulum membrane tubules are distributed by microtubules in living cells using three distinct mechanisms. *Current Biology* **8**, 798-807 (1998).

36. Wray, S. & Burdyga, T. Sarcoplasmic reticulum function in smooth muscle. *Physiological reviews* **90**, 113-178 (2010).

37. Wu, Y. *et al.* Contacts between the endoplasmic reticulum and other membranes in neurons. *Proceedings of the National Academy of Sciences*, 201701078 (2017).

38. Schauer, K. *et al.* Probabilistic density maps to study global endomembrane organization. *nAture methods* **7**, 560-566 (2010).

39. Versaevel, M., Grevesse, T. & Gabriele, S. Spatial coordination between cell and nuclear shape within micropatterned endothelial cells. *Nature communications* **3**, 671 (2012).

40. Ehlert, F.J. Contractile role of M 2 and M 3 muscarinic receptors in gastrointestinal, airway and urinary bladder smooth muscle. *Life sciences* **74**, 355-366 (2003).

41. Mundell, S.J. & Kelly, E. The effect of inhibitors of receptor internalization on the desensitization and resensitization of three Gs-coupled receptor responses. *British journal of pharmacology* **125**, 1594-1600 (1998).

42. Hansen, S.H., Sandvig, K. & Van Deurs, B. Clathrin and HA2 adaptors: effects of potassium depletion, hypertonic medium, and cytosol acidification. *The Journal of cell biology* **121**, 61-72 (1993).

43. Heuser, J.E. & Anderson, R. Hypertonic media inhibit receptor-mediated endocytosis by blocking clathrin-coated pit formation. *The Journal of cell biology* **108**, 389-400 (1989).

44. Toescu, E.C. & Verkhratsky, A. The importance of being subtle: small changes in calcium homeostasis control cognitive decline in normal aging. *Aging cell* **6**, 267-273 (2007).

45. Mizuno, Y. *et al.* Myosin light chain kinase activation and calcium sensitization in smooth muscle in vivo. *American Journal of Physiology-Cell Physiology* **295**, C358-C364 (2008).

46. Isotani, E. *et al.* Real-time evaluation of myosin light chain kinase activation in smooth muscle tissues from a transgenic calmodulin-biosensor mouse. *Proceedings of the National Academy of Sciences of the United States of America* **101**, 6279-6284 (2004).

47. George, J. *et al.* The contractile strength of vascular smooth muscle myocytes is shape dependent. *Integrative Biology* **6**, 152-163 (2014).

48. Alford, P.W., Nesmith, A.P., Seywerd, J.N., Grosberg, A. & Parker, K.K. Vascular smooth muscle contractility depends on cell shape. *Integrative Biology* **3**, 1063-1070 (2011).

49. Crabtree, G.R. Calcium, calcineurin, and the control of transcription. *Journal of Biological Chemistry* **276**, 2313-2316 (2001).

50. Sotiropoulos, A., Gineitis, D., Copeland, J. & Treisman, R. Signal-regulated activation of serum response factor is mediated by changes in actin dynamics. *Cell* **98**, 159-169 (1999).

51. Liu, H.W. *et al.* The RhoA/Rho kinase pathway regulates nuclear localization of serum response factor. *American journal of respiratory cell and molecular biology* **29**, 39-47 (2003).

52. Creemers, E.E., Sutherland, L.B., Oh, J., Barbosa, A.C. & Olson, E.N. Coactivation of MEF2 by the SAP domain proteins myocardin and MASTR. *Molecular cell* **23**, 83-96 (2006).

53. Voeltz, G.K., Rolls, M.M. & Rapoport, T.A. Structural organization of the endoplasmic reticulum. *EMBO reports* **3**, 944-950 (2002).

54. Azeloglu, E.U. & Iyengar, R. Good practices for building dynamical models in systems biology. *Sci. Signal.* **8**, fs8-fs8 (2015).

55. Wittmann, M. *et al.* Synaptic activity induces dramatic changes in the geometry of the cell nucleus: interplay between nuclear structure, histone H3 phosphorylation, and nuclear calcium signaling. *Journal of Neuroscience* **29**, 14687-14700 (2009).

56. Queisser, G., Wiegert, S. & Bading, H. Structural dynamics of the cell nucleus. *Nucleus* **2**, 98-104 (2011).

57. Mauger, J.P. Role of the nuclear envelope in calcium signalling. *Biology of the Cell* **104**, 70-83 (2012).

58. Bakal, C., Aach, J., Church, G. & Perrimon, N. Quantitative morphological signatures define local signaling networks regulating cell morphology. *science* **316**, 1753-1756 (2007).

59. Sailem, H., Bousgouni, V., Cooper, S. & Bakal, C. Cross-talk between Rho and Rac GTPases drives deterministic exploration of cellular shape space and morphological heterogeneity. *Open biology* **4**, 130132 (2014).

60. Ross, R. Cell biology of atherosclerosis. *Annual review of physiology* **57**, 791-804 (1995).

61. Dickinson, G.D., Ellefsen, K.L., Dawson, S.P., Pearson, J.E. & Parker, I. Hindered cytoplasmic diffusion of inositol trisphosphate restricts its cellular range of action. *Sci. Signal.* **9**, ra108-ra108 (2016).

62. Mitra, A. *et al.* Cell geometry dictates TNFα-induced genome response. *Proceedings of the National Academy of Sciences* **114**, E3882-E3891 (2017).

63. Jain, N., Iyer, K.V., Kumar, A. & Shivashankar, G. Cell geometric constraints induce modular gene-expression patterns via redistribution of HDAC3 regulated by actomyosin contractility. *Proceedings of the National Academy of Sciences* **110**, 11349-11354 (2013).

64. Hassinger, J.E., Oster, G., Drubin, D.G. & Rangamani, P. Design principles for robust vesiculation in clathrin-mediated endocytosis. *Proceedings of the National Academy of Sciences* **114**, E1118-E1127 (2017).

65. Sriram, K., Laughlin, J.G., Rangamani, P. & Tartakovsky, D.M. Shear-induced nitric oxide production by endothelial cells. *Biophysical Journal* **111**, 208-221 (2016).

66. Chabanon, M., Stachowiak, J.C. & Rangamani, P. Systems biology of cellular membranes: a convergence with biophysics. *Wiley Interdisciplinary Reviews: Systems Biology and Medicine* (2017).

67. Rangamani, P., Levy, M.G., Khan, S. & Oster, G. Paradoxical signaling regulates structural plasticity in dendritic spines. *Proceedings of the National Academy of Sciences* **113**, E5298-E5307 (2016).

68. Qin, D., Xia, Y. & Whitesides, G.M. Soft lithography for micro-and nanoscale patterning. *Nature protocols* **5**, 491-502 (2010).

69. Calizo, R.C. & Scarlata, S. A role for G-proteins in directing G-protein-coupled receptor–caveolae localization. *Biochemistry* **51**, 9513-9523 (2012).

70. Hanson, H.H., Reilly, J.E., Lee, R., Janssen, W.G. & Phillips, G.R. Streamlined embedding of cell monolayers on gridded glass-bottom imaging dishes for correlative light and electron microscopy. *Microscopy and Microanalysis* **16**, 747-754 (2010).

71. Atay, O. & Skotheim, J.M. Spatial and temporal signal processing and decision making by MAPK pathways. *J Cell Biol*, jcb. 201609124 (2017).

72. Kreyszig, E. *Introduction to differential geometry and Riemannian geometry*, Vol. 16. (University of Toronto Press, 1968).

73. Cooling, M., Hunter, P. & Crampin, E.J. Modeling hypertrophic IP3 transients in the cardiac myocyte. *Biophysical journal* **93**, 3421-3433 (2007).

74. Vollmer, J., Menshykau, D. & Iber, D. Simulating organogenesis in COMSOL: cell-based signaling models. *arXiv preprint arXiv:1309.6479* (2013).

75. Loew, L.M. & Schaff, J.C. The Virtual Cell: a software environment for computational cell biology. *Trends in biotechnology* **19**, 401-406 (2001).

76. Li, Y.-X. & Rinzel, J. Equations for InsP 3 receptor-mediated [Ca 2+] i oscillations derived from a detailed kinetic model: a Hodgkin-Huxley like formalism. *Journal of theoretical Biology* **166**, 461-473 (1994).

77. Fink, C.C. *et al.* An image-based model of calcium waves in differentiated neuroblastoma cells. *Biophysical Journal* **79**, 163-183 (2000).

78. De Young, G.W. & Keizer, J. A single-pool inositol 1, 4, 5-trisphosphate-receptor-based model for agonist-stimulated oscillations in Ca2+ concentration. *Proceedings of the National Academy of Sciences* **89**, 9895-9899 (1992).

79. Wagner, J. & Keizer, J. Effects of rapid buffers on Ca2+ diffusion and Ca2+ oscillations. *Biophysical Journal* **67**, 447 (1994).

80. Lukas, T.J. A signal transduction pathway model prototype I: from agonist to cellular endpoint. *Biophysical journal* **87**, 1406-1416 (2004).

81. Maurya, M.R. & Subramaniam, S. A kinetic model for calcium dynamics in RAW 264.7 cells: 1. Mechanisms, parameters, and subpopulational variability. *Biophysical journal* **93**, 709-728 (2007).

82. Keener, J.P. & Sneyd, J. *Mathematical physiology*, Vol. 1. (Springer, 1998).

83. Wiesner, T.F., Berk, B.C. & Nerem, R.M. A mathematical model of cytosolic calcium dynamics in human umbilical vein endothelial cells. *American Journal of Physiology-Cell Physiology* **270**, C1556-C1569 (1996).

84. Knot, H.J. & Nelson, M.T. Regulation of arterial diameter and wall [Ca2+] in cerebral arteries of rat by membrane potential and intravascular pressure. *The Journal of physiology* **508**, 199-209 (1998).

85. Fink, C.C. *et al.* Morphological control of inositol-1, 4, 5-trisphosphate–dependent signals. *The Journal of cell biology* **147**, 929-936 (1999).

86. Bers, D. *Excitation-contraction coupling and cardiac contractile force*, Vol. 237. (Springer Science & Business Media, 2001).

87. Xu, C., Watras, J. & Loew, L.M. Kinetic analysis of receptor-activated phosphoinositide turnover. *The Journal of cell biology* **161**, 779-791 (2003).

88. Golebiewska, U. *et al.* Membrane-bound basic peptides sequester multivalent (PIP 2), but not monovalent (PS), acidic lipids. *Biophysical journal* **91**, 588-599 (2006).

89. Eungdamrong, N.J. & Iyengar, R. Compartment-specific feedback loop and regulated trafficking can result in sustained activation of Ras at the Golgi. *Biophysical journal* **92**, 808-815 (2007).